



Available online at www.sciencedirect.com

ScienceDirect

Comput. Methods Appl. Mech. Engrg. 377 (2021) 113691

**Computer methods
in applied
mechanics and
engineering**

www.elsevier.com/locate/cma

An asymptotically compatible treatment of traction loading in linearly elastic peridynamic fracture

Yue Yu^{a,*}, Huaiqian You^a, Nathaniel Trask^b

^a Department of Mathematics, Lehigh University, Bethlehem, PA, United States of America

^b Center for Computing Research, Sandia National Laboratories, Albuquerque, NM, United States of America

Received 26 September 2020; received in revised form 5 January 2021; accepted 16 January 2021

Available online 2 February 2021

Abstract

Meshfree discretizations of state-based peridynamic models are attractive due to their ability to naturally describe fracture of general materials. However, two factors conspire to prevent meshfree discretizations of state-based peridynamics from converging to corresponding local solutions as resolution is increased: quadrature error prevents an accurate prediction of bulk mechanics, and the lack of an explicit boundary representation presents challenges when applying traction loads. In this paper, we develop a reformulation of the linear peridynamic solid (LPS) model to address these shortcomings, using improved meshfree quadrature, a reformulation of the nonlocal dilatation, and a consistent handling of the nonlocal traction condition to construct a model with rigorous accuracy guarantees. In particular, these improvements are designed to enforce discrete consistency in the presence of evolving fractures, whose *a priori* unknown location render consistent treatment difficult. In the absence of fracture, when a corresponding classical continuum mechanics model exists, our improvements provide asymptotically compatible convergence to corresponding local solutions, eliminating surface effects and issues with traction loading which have historically plagued peridynamic discretizations. When fracture occurs, our formulation automatically provides a sharp representation of the fracture surface by breaking bonds, avoiding the loss of mass. We provide rigorous error analysis and demonstrate convergence for a number of benchmarks, including manufactured solutions, free-surface, nonhomogeneous traction loading, and composite material problems. Finally, we validate simulations of brittle fracture against a recent experiment of dynamic crack branching in soda-lime glass, providing evidence that the scheme yields accurate predictions for practical engineering problems.

© 2021 Elsevier B.V. All rights reserved.

Keywords: Peridynamics; Neumann boundary condition; Fracture; Asymptotic compatibility; Meshfree method; Nonlocal models

1. Introduction

Peridynamics provides a description of continuum mechanics in terms of integral operators rather than classical differential operators [1–7]. These nonlocal models are defined in terms of a lengthscale δ , referred to as a horizon, which denotes the extent of nonlocal interaction. The nonlocal viewpoint allows a natural description of processes requiring reduced regularity in the relevant solution, such as fracture mechanics [8,9]. An important feature of such

* Corresponding author.

E-mail addresses: yuy214@lehigh.edu (Y. Yu), huy316@lehigh.edu (H. You), natrask@sandia.gov (N. Trask).

models is that when classical continuum models still apply, they revert back to classical continuum models as $\delta \rightarrow 0$. Discretizations which preserve this limit under refinement $h \rightarrow 0$ are termed asymptotically compatible (AC) [10], and there has been significant work in recent years toward establishing such discretizations — for an incomplete list see [10–20]. Broadly, strategies either involve adopting traditional finite element shape functions and carefully performing geometric calculations to integrate over relevant horizon/element subdomains, or adopt a strong-form meshfree discretization where particles are associated with abstract measure. The former is more amenable to mathematical analysis due to a better variational setting, while the latter is simple to implement and generally faster [21,22]. In this paper we pursue the meshfree viewpoint.

For fracture mechanics problems one often refines both δ and h at the same rate under so-called M-convergence, $\delta = Mh$, for $M > 0$ [23]. In this setting, one obtains banded stiffness matrices allowing scalable implementations. Typically in the literature a scheme is termed AC if it recovers the solution in both the finite δ and M-convergence limit — in this work we abuse the definition slightly and only require the M-convergence case for asymptotic compatibility as the relevant limit for problems with a corresponding local limit. This AC property is only one necessary ingredient in achieving a convergent simulation, and our recent work focused upon establishing convergence in this setting for boundary value problems [18,19]. To achieve similar convergence for problems involving fracture, one must also consider the interplay between consistency of quadrature for discrete operators and the imposition of traction loads as fracture surfaces open up and evolve [24]. For peridynamic fracture problems where the free surface evolves implicitly via the breaking of bonds [17,25], one lacks an explicit boundary representation over the course of a simulation. In addition to providing challenges regarding accurate imposition of traction loads, the breaking of bonds also renders higher-order numerical quadrature inaccurate, as consistent AC quadrature weights are typically derived in the absence of damage.

Our goal is to provide a comprehensive treatment of fracture, nonlocal quadrature, and traction loading which is able to perform more accurate state-based peridynamic fracture simulations free of spurious surface effects. In particular, when no fracture occurs and therefore the classical continuum theory applies, the formulation should preserve the AC limit under M-convergence. When fracture occurs, the formulation should be able to capture the material damage and the evolving fracture surfaces via bond breaking. This practically means that one is able to incorporate all of the necessary ingredients to perform non-trivial simulations of fracture mechanics while maintaining a scalable implementation and guaranteeing convergence. Such a capability is elusive in the peridynamic literature; while peridynamics has been shown to provide a powerful modeling platform for a broad range of applications [26,27], the development of efficient discretizations with rigorous underpinnings has lagged behind until the last few years.

The challenge in incorporating traction loading into a peridynamic framework stems from the fact that, in contrast to local mechanics, peridynamic boundary conditions must be defined on a finite volume region outside the surface [9,20,28]. Theoretical and numerical challenges arise in how to mathematically impose nonhomogeneous Neumann boundary conditions properly in the nonlocal model. In peridynamic models, careless imposition of traction loads leads to a smaller effective material stiffness close to the boundary, since the integral on those material points is over a smaller region. Therefore, an unphysical strain energy concentration is induced, leading in turn to an artificial softening of the material near the boundary. Such undesirable phenomena are referred to in the literature as a “surface” or “skin” effects [29,30]. We propose a novel treatment of nonlocal traction-type boundary conditions which avoid the surface effect by designing a loading aimed to recover the corresponding local traction boundary condition as $\delta \rightarrow 0$. The approach requires no explicit representation of the boundary, imposing the traction volumetrically using the same information that would be available during a traditional meshfree bond-based peridynamics simulation. Although the Neumann-constrained nonlocal problem and its AC limit were investigated in nonlocal diffusion models [18–20,28,31,32], to the authors’ best knowledge, the development of AC peridynamic formulations with traction-type boundary conditions remains restricted to weak formulations, simple traction loadings and/or simple geometries. Several modeling and numerical approaches have been proposed to correct the surface effect [7,33–39] but mostly restricted to free surfaces. For nonzero loadings, the tractions are often applied as prescribed body forces through a layer of finite thickness at the material boundary [27,33,40], as a surface integral through a weak form [41], or by modifying the nonlocal operator through eigenvalues analysis [42]. Therefore, developing an AC meshfree discretization method for peridynamics which is capable to handle nonhomogeneous traction loadings on complex boundaries is critical for the general practice of peridynamics in realistic engineering applications.

We consider the linear peridynamic solid (LPS) model [43] as a prototypical state-based model appropriate for brittle fracture. The LPS model may be interpreted as a nonlocal generalization of the mixed form of linear elasticity, evolving both displacements and a dilatation. We will show that consistent treatment evolving traction loading will require a modification to the definition of dilatation to guarantee consistency in the presence of fractures; conceptually this corresponds to the fact that dilatation is a kinematic variable without associated boundary conditions, and should be estimated consistently independently of whether a fracture is occurring in the vicinity of a given point. Based on the modified nonlocal dilatation, we further propose a new nonlocal generalization of classical traction loads in the LPS model. Particularly, we convert the local traction loads to a correction term in the momentum balance equation, which provides an estimate for the nonlocal interactions of each material point with points outside the domain. Based on this traction-type boundary condition, a meshfree formulation is developed for the LPS model based on the optimization-based quadrature rule [17], which preserves the AC limit under M-convergence and naturally represents the evolving free surfaces in dynamic fracture problems. We note that asymptotic compatibility is not well-defined for dynamic fracture, as there is no known corresponding local theory for peridynamics with bond breaking.¹ However, our modified LPS formulation preserves the AC limit for the linear elastic model with traction loading on the evolving fracture surfaces. This fact, together with the consistent discretization introduced here, provides the opportunity for efficient and accurate peridynamic fracture simulations.

We remark that the paper is organized to first establish the rigorous mathematical underpinnings of the approach, while the second half focuses on a more engineering-oriented exploration of its application. Readers with more applied interests may skip many of the proofs in the work without issue. The work is organized as follows. We recall first the linear peridynamic solid (LPS) model definition in Section 2. In Section 3.1, we introduce a novel approach to apply classical traction loads on the LPS model. After establishing the continuous limits of the scheme, we next pursue a consistent discretization. In Section 4 we introduce meshfree quadrature which preserves asymptotic compatibility in the $\delta \rightarrow 0$ limit, and establish the discrete scheme for boundary value problems in the absence of fracture. We proceed to investigate a number of two-dimensional statics problems with analytic solutions for the local limit in Section 5. These test cases include: linear patch tests (Section 5.1); manufactured local limits to illustrate asymptotic convergence rates (Section 5.2); homogeneous materials with free-surfaces or non-zero traction loading on curvilinear surfaces (Section 5.3); composite materials with internal interfaces (Section 5.4). In Section 6, we further extend the proposed formulation to handle dynamic brittle fracture, and provide preliminary validation results by comparing our numerical results with available numerical simulations and experimental measurements on three benchmark problems. Section 7 summarizes our findings and discusses future research.

2. A linear state-based peridynamic model

We consider the state-based linear peridynamic solid (LPS) model in a body occupying the domain $\Omega \subset \mathbb{R}^d$, $d = 2$ or 3. Let θ be the nonlocal dilatation, generalizing the local divergence of displacement, and $K(r)$ denote a positive radial function with compactly supported on the δ -ball $B_\delta(\mathbf{x})$. The momentum balance and nonlocal dilatation are then given by the following,

$$\mathcal{L}_\delta \mathbf{u} := -\frac{C_\alpha}{m(\delta)} \int_{B_\delta(\mathbf{x})} (\lambda - \mu) K(|\mathbf{y} - \mathbf{x}|) (\mathbf{y} - \mathbf{x}) (\theta(\mathbf{x}) + \theta(\mathbf{y})) d\mathbf{y} \quad (2.1)$$

$$-\frac{C_\beta}{m(\delta)} \int_{B_\delta(\mathbf{x})} \mu K(|\mathbf{y} - \mathbf{x}|) \frac{(\mathbf{y} - \mathbf{x}) \otimes (\mathbf{y} - \mathbf{x})}{|\mathbf{y} - \mathbf{x}|^2} (\mathbf{u}(\mathbf{y}) - \mathbf{u}(\mathbf{x})) d\mathbf{y} = \mathbf{f}(\mathbf{x}),$$

$$\theta(\mathbf{x}) := \frac{d}{m(\delta)} \int_{B_\delta(\mathbf{x})} K(|\mathbf{y} - \mathbf{x}|) (\mathbf{y} - \mathbf{x}) \cdot (\mathbf{u}(\mathbf{y}) - \mathbf{u}(\mathbf{x})) d\mathbf{y}, \quad (2.2)$$

where $\mathbf{u} \in \mathbb{R}^d$ denotes the displacement, $\mathbf{f} \in \mathbb{R}^d$ denotes the body load, the weighted volume

$$m(\delta) := \int_{B_\delta(\mathbf{x})} K(|\mathbf{y} - \mathbf{x}|) |\mathbf{y} - \mathbf{x}|^2 d\mathbf{y},$$

and μ, λ denote the shear and Lame modulus, respectively. With appropriate choice of scaling parameters $C_\alpha > 0$, $C_\beta > 0$ and the weighting function $K(r)$, it can be shown that the system converges to the Navier equations [47–49]:

$$\mathcal{L}_0 \mathbf{u} := -\nabla \cdot (\lambda \text{tr}(\mathbf{E}) \mathbf{I} + 2\mu \mathbf{E}) = -(\lambda - \mu) \nabla [\text{tr}(\mathbf{E})] - \mu \nabla \cdot (2\mathbf{E} + \text{tr}(\mathbf{E}) \mathbf{I}) = \mathbf{f}, \quad (2.3)$$

¹ There is an emerging theory of local fracture modeling that is approached by peridynamic models with bond softening, see [24,44–46].

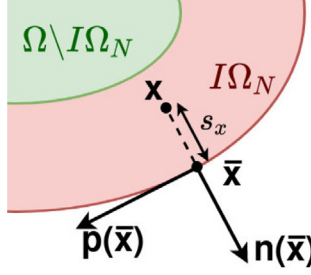


Fig. 1. Notations for the projection of point $\mathbf{x} \in \mathcal{I}\Omega$, the corresponding unit tangential vector $\mathbf{p}(\bar{\mathbf{x}})$ and the unit normal vector $\mathbf{n}(\bar{\mathbf{x}})$.

where the strain tensor $\mathbf{E} := \frac{1}{2}(\nabla \mathbf{u} + (\nabla \mathbf{u})^T)$ and we note that $\text{tr}(\mathbf{E}) = \nabla \cdot \mathbf{u}$. To recover parameters for 3D linear elasticity, $C_\alpha = 3$, $C_\beta = 30$. For 2D problems, $C_\alpha = 2$, $C_\beta = 16$. In this paper we consider 2D problems ($d = 2$) and the following popular scaled kernel:

$$K(r) = \begin{cases} \frac{1}{r}, & \text{for } r \leq \delta; \\ 0, & \text{for } r > \delta, \end{cases} \quad \frac{K(r)}{m(\delta)} = \begin{cases} \frac{3}{2\pi\delta^3 r}, & \text{for } r \leq \delta; \\ 0, & \text{for } r > \delta. \end{cases} \quad (2.4)$$

although the idea may be generalized to more general kernels and 3D cases. As shown in [49], we can define the nonlocal strain energy density as

$$W_\delta(\mathbf{u}) = \frac{C_\alpha d (\lambda - \mu)}{(m(\delta))^2} \int_{\Omega} \left[\int_{B_\delta(\mathbf{x})} K(|\mathbf{y} - \mathbf{x}|) (\mathbf{y} - \mathbf{x}) \cdot (\mathbf{u}(\mathbf{y}) - \mathbf{u}(\mathbf{x})) d\mathbf{y} \right]^2 d\mathbf{x} \\ + \frac{C_\beta \mu}{2m(\delta)} \int_{\Omega} \left[\int_{B_\delta(\mathbf{x})} \frac{K(|\mathbf{y} - \mathbf{x}|)}{|\mathbf{y} - \mathbf{x}|^2} [(\mathbf{u}(\mathbf{y}) - \mathbf{u}(\mathbf{x})) \cdot (\mathbf{y} - \mathbf{x})]^2 d\mathbf{y} \right] d\mathbf{x},$$

and the energy space $S_\delta(\Omega)$ as

$$S_\delta(\Omega) := \left\{ \mathbf{u} \in L^2(\Omega) : |\mathbf{u}|_{S_\delta(\Omega)} := \frac{1}{m(\delta)} \int_{\Omega} \int_{\Omega} \frac{K(|\mathbf{y} - \mathbf{x}|)}{|\mathbf{y} - \mathbf{x}|^2} [(\mathbf{u}(\mathbf{y}) - \mathbf{u}(\mathbf{x})) \cdot (\mathbf{y} - \mathbf{x})]^2 d\mathbf{y} d\mathbf{x} < \infty \right\}.$$

Note that $|\mathbf{u}|_{S_\delta(\Omega)} = 0$ if and only if \mathbf{u} represents an infinitesimally rigid displacement, i.e.:

$$\mathbf{u}(\mathbf{x}) \in \Pi := \{ \mathbf{Q}\mathbf{x} + \mathbf{b}, \mathbf{Q} \in \mathbb{R}^{d \times d}, \mathbf{Q}^T = -\mathbf{Q}, \mathbf{b} \in \mathbb{R}^d \}.$$

3. Neumann and mixed-type constraint problems

We now consider a state-based peridynamic problem with general mixed boundary conditions: $\partial\Omega = \partial\Omega_D \cup \partial\Omega_N$ and $(\partial\Omega_D)^o \cap (\partial\Omega_N)^o = \emptyset$. Here $\partial\Omega_D$ and $\partial\Omega_N$ are both 1D curves. We denote the regions near the boundary $\partial\Omega$ as

$$\mathcal{I}\Omega := \{ \mathbf{x} \in \Omega | \text{dist}(\mathbf{x}, \partial\Omega) < \delta \}, \mathcal{B}\Omega := \{ \mathbf{x} \notin \Omega | \text{dist}(\mathbf{x}, \partial\Omega) < \delta \}, \mathcal{BB}\Omega := \{ \mathbf{x} \notin \Omega | \text{dist}(\mathbf{x}, \partial\Omega) < 2\delta \}.$$

Note that to apply the nonlocal Dirichlet-type boundary condition, $\mathbf{u}(\mathbf{x}) = \mathbf{u}_D(\mathbf{x})$ is required in a layer with non-zero volume outside Ω , while the proposed traction load is applied as a Neumann boundary condition on the sharp interface $\partial\Omega_N$. To define a Dirichlet-type constraint, we denote

$$\mathcal{I}\Omega_D := \{ \mathbf{x} \in \Omega | \text{dist}(\mathbf{x}, \partial\Omega_D) < \delta \}, \mathcal{B}\Omega_D := \{ \mathbf{x} \notin \Omega | \text{dist}(\mathbf{x}, \partial\Omega_D) < \delta \}, \mathcal{BB}\Omega_D := \{ \mathbf{x} \notin \Omega | \text{dist}(\mathbf{x}, \partial\Omega_D) < 2\delta \},$$

and assume that the value of \mathbf{u} is given on $\mathcal{BB}\Omega_D$. Similarly, to apply the Neumann constraint, we denote

$$\mathcal{I}\Omega_N := \{ \mathbf{x} \in \Omega | \text{dist}(\mathbf{x}, \partial\Omega_N) < \delta \}, \mathcal{B}\Omega_N := \{ \mathbf{x} \notin \Omega | \text{dist}(\mathbf{x}, \partial\Omega_N) < \delta \}, \mathcal{BB}\Omega_N := \{ \mathbf{x} \notin \Omega | \text{dist}(\mathbf{x}, \partial\Omega_N) < 2\delta \}.$$

Unless stated otherwise, in this paper we further assume sufficient regularity in the boundary that we may take δ sufficiently small so that for any $\mathbf{x} \in \mathcal{I}\Omega_N$ (see Fig. 1 for illustration), there exists a unique orthogonal projection of \mathbf{x} onto $\partial\Omega_N$. We denote this projection as $\bar{\mathbf{x}}$. Therefore, one has $\bar{\mathbf{x}} - \mathbf{x} = s_x \mathbf{n}(\bar{\mathbf{x}})$ for $\mathbf{x} \in \mathcal{I}\Omega_N$, where $0 < s_x < \delta$. Here \mathbf{n} denotes the normal direction pointing out of the domain for each $\mathbf{x} \in \mathcal{I}\Omega_N$, and \mathbf{p} denotes the tangential

direction. Moreover, we employ the following notations for the directional components of the Hessian matrix of a scalar function v :

$$[v(\mathbf{x})]_{pp} := \mathbf{p}^T(\bar{\mathbf{x}}) \nabla^2 v(\mathbf{x}) \mathbf{p}(\bar{\mathbf{x}}), \quad [v(\mathbf{x})]_{nn} := \mathbf{n}^T(\bar{\mathbf{x}}) \nabla^2 v(\mathbf{x}) \mathbf{n}(\bar{\mathbf{x}}), \quad [v(\mathbf{x})]_{pn} := \mathbf{p}^T(\bar{\mathbf{x}}) \nabla^2 v(\mathbf{x}) \mathbf{n}(\bar{\mathbf{x}}).$$

3.1. Formulation for non-homogeneous traction loading

In this section, we consider an LPS model subject to local traction loads on the sharp interface $\partial\Omega_N$, by developing nonlocal Neumann constraint formulation with proper correction terms for $\mathbf{x} \in \mathcal{I}\Omega_N$.

Firstly, we propose a corrected formulation for the nonlocal dilatation θ in (2.2). When $\mathbf{u} \in C^1(\Omega)$ and $B_\delta(\mathbf{x}) \setminus \Omega = \emptyset$, the definition of $\theta(\mathbf{x})$ limits to a local divergence operator $\nabla \cdot \mathbf{u}(\mathbf{x})$ as $\delta \rightarrow 0$ by taking the Taylor series expansion of \mathbf{u} as $\mathbf{u}(\mathbf{y}) = \mathbf{u}(\mathbf{x}) + \nabla \mathbf{u}(\mathbf{x}) \cdot (\mathbf{y} - \mathbf{x}) + O(\delta^2)$ and employing a symmetry argument. However, for $\mathbf{x} \in \mathcal{I}\Omega_N$ the domain of integration is non-spherical due to proximity to the boundary, and the loss of symmetry results in an inconsistent θ . Thus, surface-effects manifest in the definition of dilatation before any modeling assumptions are made regarding the material response. To address the surface-effect we modify the definition of nonlocal dilatation in (2.2) to enforce consistency for linear displacement fields, independent of whether the horizon intersects the boundary of the domain. In the spirit of correspondence models and corrected smoothed particle hydrodynamics (SPH) schemes [50], we introduce a correction tensor $\mathbf{M}(\mathbf{x})$ to (2.2):

$$\theta^{corr}(\mathbf{x}) = \frac{d}{m(\delta)} \int_{B_\delta(\mathbf{x}) \cap \Omega} K(|\mathbf{y} - \mathbf{x}|) (\mathbf{y} - \mathbf{x}) \cdot \mathbf{M}(\mathbf{x}) \cdot (\mathbf{u}(\mathbf{y}) - \mathbf{u}(\mathbf{x})) d\mathbf{y}, \quad (3.1)$$

$$\mathbf{M}(\mathbf{x}) = \left[\frac{d}{m(\delta)} \int_{B_\delta(\mathbf{x}) \cap \Omega} K(|\mathbf{y} - \mathbf{x}|) (\mathbf{y} - \mathbf{x}) \otimes (\mathbf{y} - \mathbf{x}) d\mathbf{y} \right]^{-1}. \quad (3.2)$$

Note that for $\mathbf{x} \in \Omega \setminus \mathcal{I}\Omega_N$, $\mathbf{M}(\mathbf{x})$ reverts to the identity matrix and (3.1) reverts to (2.2). With a slight abuse of notation, we denote $\theta^{corr}(\mathbf{x})$ as θ in the remainder. In the next section, we will further show that for sufficiently smooth domain Ω and $\mathbf{u} \in C^1(\Omega)$, the modified dilatation is well-posed and consistent with the local dilatation.

We next introduce a Neumann constraint to impose a traction load \mathbf{T} on $\partial\Omega_N$ by modifying the state-peridynamic peridynamic model (2.1) in $\mathcal{I}\Omega_N$. Denoting T_p and T_n as the tangential and normal components of \mathbf{T} , respectively, we propose the following formulation:

$$\begin{aligned} \mathcal{L}_{N\delta} \mathbf{u}(\mathbf{x}) &:= -\frac{C_\alpha}{m(\delta)} \int_{B_\delta(\mathbf{x}) \cap \Omega} (\lambda - \mu) K(|\mathbf{y} - \mathbf{x}|) (\mathbf{y} - \mathbf{x}) (\theta(\mathbf{x}) + \theta(\mathbf{y})) d\mathbf{y} \\ &\quad - \frac{C_\beta}{m(\delta)} \int_{B_\delta(\mathbf{x}) \cap \Omega} \mu K(|\mathbf{y} - \mathbf{x}|) \frac{(\mathbf{y} - \mathbf{x}) \otimes (\mathbf{y} - \mathbf{x})}{|\mathbf{y} - \mathbf{x}|^2} (\mathbf{u}(\mathbf{y}) - \mathbf{u}(\mathbf{x})) d\mathbf{y} \\ &\quad - \frac{2C_\alpha \theta(\mathbf{x})}{m(\delta)} \int_{B_\delta(\mathbf{x}) \setminus \Omega} (\lambda - \mu) K(|\mathbf{y} - \mathbf{x}|) (\mathbf{y} - \mathbf{x}) d\mathbf{y} \\ &\quad - \frac{C_\beta \theta(\mathbf{x})}{2m(\delta)} \int_{B_\delta(\mathbf{x}) \setminus \Omega} (\lambda + 2\mu) K(|\mathbf{y} - \mathbf{x}|) \frac{[(\mathbf{y} - \mathbf{x}) \cdot \mathbf{n}] [(\mathbf{y} - \mathbf{x}) \cdot \mathbf{p}]^2}{|\mathbf{y} - \mathbf{x}|^2} \mathbf{n} d\mathbf{y} \\ &\quad + \frac{C_\beta \theta(\mathbf{x})}{2m(\delta)} \int_{B_\delta(\mathbf{x}) \setminus \Omega} \lambda K(|\mathbf{y} - \mathbf{x}|) \frac{[(\mathbf{y} - \mathbf{x}) \cdot \mathbf{n}]^3}{|\mathbf{y} - \mathbf{x}|^2} \mathbf{n} d\mathbf{y} \\ &= \mathbf{f}(\mathbf{x}) + \frac{C_\beta}{m(\delta)} \int_{B_\delta(\mathbf{x}) \setminus \Omega} K(|\mathbf{y} - \mathbf{x}|) \frac{[(\mathbf{y} - \mathbf{x}) \cdot \mathbf{n}]}{|\mathbf{y} - \mathbf{x}|^2} [(\mathbf{y} - \mathbf{x}) \cdot \mathbf{p}]^2 [T_p(\bar{\mathbf{x}}) \mathbf{p}] d\mathbf{y} \\ &\quad + \frac{C_\beta}{2m(\delta)} \int_{B_\delta(\mathbf{x}) \setminus \Omega} K(|\mathbf{y} - \mathbf{x}|) \frac{[(\mathbf{y} - \mathbf{x}) \cdot \mathbf{n}]}{|\mathbf{y} - \mathbf{x}|^2} \left([(\mathbf{y} - \mathbf{x}) \cdot \mathbf{n}]^2 - [(\mathbf{y} - \mathbf{x}) \cdot \mathbf{p}]^2 \right) [T_n(\bar{\mathbf{x}}) \mathbf{n}] d\mathbf{y} \\ &:= \mathbf{f}_{N\delta}(\mathbf{x}), \end{aligned} \quad (3.3)$$

where $\bar{\mathbf{x}}$ is the projection of \mathbf{x} on the boundary. In the next section, we will show that this formulation provides an approximation for the corresponding linear elastic model with local traction loadings in the case of linear displacement fields.

To summarize, we obtain a formulation for a static state-based peridynamic problem with general mixed boundary conditions:

$$\begin{cases} \mathcal{L}_\delta \mathbf{u}(\mathbf{x}) = \mathbf{f}(\mathbf{x}), & \text{in } \Omega \setminus \mathcal{I}\Omega_N \\ \mathcal{L}_{N\delta} \mathbf{u}(\mathbf{x}) = \mathbf{f}_{N\delta}(\mathbf{x}), & \text{in } \mathcal{I}\Omega_N \\ \theta(\mathbf{x}) = \frac{d}{m(\delta)} \int_{B_\delta(\mathbf{x})} K(|\mathbf{y} - \mathbf{x}|)(\mathbf{y} - \mathbf{x})^T (\mathbf{u}(\mathbf{y}) - \mathbf{u}(\mathbf{x})) d\mathbf{y}, & \text{in } \Omega \cup \mathcal{B}\Omega_D \setminus \mathcal{I}\Omega_N \\ \theta(\mathbf{x}) = \frac{d}{m(\delta)} \int_{B_\delta(\mathbf{x}) \cap \Omega} K(|\mathbf{y} - \mathbf{x}|)(\mathbf{y} - \mathbf{x})^T \mathbf{M}(\mathbf{x}) (\mathbf{u}(\mathbf{y}) - \mathbf{u}(\mathbf{x})) d\mathbf{y}, & \text{in } \mathcal{I}\Omega_N \\ \mathbf{u}(\mathbf{x}) = \mathbf{u}_D(\mathbf{x}), & \text{in } \mathcal{B}\mathcal{B}\Omega_D \end{cases} \quad (3.4)$$

where the correction tensor is defined as

$$\mathbf{M} := \left[\frac{d}{m(\delta)} \int_{B_\delta(\mathbf{x}) \cap \Omega} K(|\mathbf{y} - \mathbf{x}|)(\mathbf{y} - \mathbf{x}) \otimes (\mathbf{y} - \mathbf{x}) d\mathbf{y} \right]^{-1},$$

and a body load $\mathbf{f}_{N\delta}$ is defined on $\mathbf{x} \in \mathcal{I}\Omega_N$ as

$$\begin{aligned} \mathbf{f}_{N\delta}(\mathbf{x}) := & \mathbf{f}(\mathbf{x}) + \frac{C_\beta}{m(\delta)} \int_{B_\delta(\mathbf{x}) \setminus \Omega} K(|\mathbf{y} - \mathbf{x}|) \frac{[(\mathbf{y} - \mathbf{x}) \cdot \mathbf{n}]}{|\mathbf{y} - \mathbf{x}|^2} [(\mathbf{y} - \mathbf{x}) \cdot \mathbf{p}]^2 [T_p(\bar{\mathbf{x}})\mathbf{p}] d\mathbf{y} \\ & + \frac{C_\beta}{2m(\delta)} \int_{B_\delta(\mathbf{x}) \setminus \Omega} K(|\mathbf{y} - \mathbf{x}|) \frac{[(\mathbf{y} - \mathbf{x}) \cdot \mathbf{n}]}{|\mathbf{y} - \mathbf{x}|^2} \left([(\mathbf{y} - \mathbf{x}) \cdot \mathbf{n}]^2 - [(\mathbf{y} - \mathbf{x}) \cdot \mathbf{p}]^2 \right) [T_n(\bar{\mathbf{x}})\mathbf{n}] d\mathbf{y}. \end{aligned}$$

3.2. Well-posedness and consistency analysis

In this section, we will show that the modified dilatation is well-posed and consistent with the local dilatation. Specifically, we prove that for sufficiently smooth domain, the correction tensor \mathbf{M} is invertible, and that for $\mathbf{u} \in C^1(\Omega)$, $\theta \rightarrow \nabla \cdot \mathbf{u}$ as $\delta \rightarrow 0$. Moreover, we will demonstrate that for linear displacement \mathbf{u} and under certain geometric assumptions, the modified formulation (3.4) is consistent with the classical linear elastic problem with traction loadings. For simplicity of notation, we indicate a generic constant independent of δ as C , and write $K(|\mathbf{y} - \mathbf{x}|)$ as K .

We first analyze existence and bounds of \mathbf{M} :

Theorem 3.1. *Given that $\Omega \in \mathbb{R}^d$ ($d = 2$) is a C^3 domain, then there exists a $\bar{\delta} > 0$ such that for $0 < \delta \leq \bar{\delta}$ the correction tensor is a well-defined symmetric matrix, and*

$$\begin{aligned} \mathbf{M} &= \begin{bmatrix} \frac{d}{m(\delta)} \int_{B_\delta(\mathbf{x}) \cap \Omega} K((\mathbf{y} - \mathbf{x}) \cdot \mathbf{p})^2 d\mathbf{y} & O(\delta^2) \\ O(\delta^2) & \frac{d}{m(\delta)} \int_{B_\delta(\mathbf{x}) \cap \Omega} K((\mathbf{y} - \mathbf{x}) \cdot \mathbf{n})^2 d\mathbf{y} \end{bmatrix}^{-1} \\ &= \begin{bmatrix} \left(\frac{d}{m(\delta)} \int_{B_\delta(\mathbf{x}) \cap \Omega} K((\mathbf{y} - \mathbf{x}) \cdot \mathbf{p})^2 d\mathbf{y} \right)^{-1} + O(\delta^4) & O(\delta^2) \\ O(\delta^2) & \left(\frac{d}{m(\delta)} \int_{B_\delta(\mathbf{x}) \cap \Omega} ((\mathbf{y} - \mathbf{x}) \cdot \mathbf{n})^2 d\mathbf{y} \right)^{-1} + O(\delta^4) \end{bmatrix}. \end{aligned}$$

Proof. To show that the correction tensor \mathbf{M} is well-defined, it suffices to show that $|det(\mathbf{M}^{-1})| > 0$. We adopt notation in Fig. 2, with a Cartesian coordinate system oriented so that $\bar{\mathbf{x}}$ coincides with the origin, and the vectors $\mathbf{p}(\bar{\mathbf{x}})$ and $\mathbf{n}(\bar{\mathbf{x}})$ are oriented along the positive x -axis and negative y -axis, respectively. We note that

$$\begin{aligned} \mathbf{M}^{-1} &= \frac{d}{m(\delta)} \begin{bmatrix} \int_{B_\delta(\mathbf{x}) \cap \Omega} K((\mathbf{y} - \mathbf{x}) \cdot \mathbf{p})^2 d\mathbf{y} & \int_{B_\delta(\mathbf{x}) \cap \Omega} K((\mathbf{y} - \mathbf{x}) \cdot \mathbf{p})((\mathbf{y} - \mathbf{x}) \cdot \mathbf{n}) d\mathbf{y} \\ \int_{B_\delta(\mathbf{x}) \cap \Omega} K((\mathbf{y} - \mathbf{x}) \cdot \mathbf{p})((\mathbf{y} - \mathbf{x}) \cdot \mathbf{n}) d\mathbf{y} & \int_{B_\delta(\mathbf{x}) \cap \Omega} K((\mathbf{y} - \mathbf{x}) \cdot \mathbf{n})^2 d\mathbf{y} \end{bmatrix} \\ &= \begin{bmatrix} 1 & 0 \\ 0 & 1 \end{bmatrix} - \frac{d}{m(\delta)} \begin{bmatrix} \int_{D_\delta} K((\mathbf{y} - \mathbf{x}) \cdot \mathbf{p})^2 d\mathbf{y} & \int_{D_\delta} K((\mathbf{y} - \mathbf{x}) \cdot \mathbf{p})((\mathbf{y} - \mathbf{x}) \cdot \mathbf{n}) d\mathbf{y} \\ \int_{D_\delta} K((\mathbf{y} - \mathbf{x}) \cdot \mathbf{p})((\mathbf{y} - \mathbf{x}) \cdot \mathbf{n}) d\mathbf{y} & \int_{D_\delta} K((\mathbf{y} - \mathbf{x}) \cdot \mathbf{n})^2 d\mathbf{y} \end{bmatrix} \\ &\quad - \frac{d}{m(\delta)} \begin{bmatrix} \int_{G_\delta} K((\mathbf{y} - \mathbf{x}) \cdot \mathbf{p})^2 d\mathbf{y} & \int_{G_\delta} K((\mathbf{y} - \mathbf{x}) \cdot \mathbf{p})((\mathbf{y} - \mathbf{x}) \cdot \mathbf{n}) d\mathbf{y} \\ \int_{G_\delta} K((\mathbf{y} - \mathbf{x}) \cdot \mathbf{p})((\mathbf{y} - \mathbf{x}) \cdot \mathbf{n}) d\mathbf{y} & \int_{G_\delta} K((\mathbf{y} - \mathbf{x}) \cdot \mathbf{n})^2 d\mathbf{y} \end{bmatrix}. \end{aligned}$$

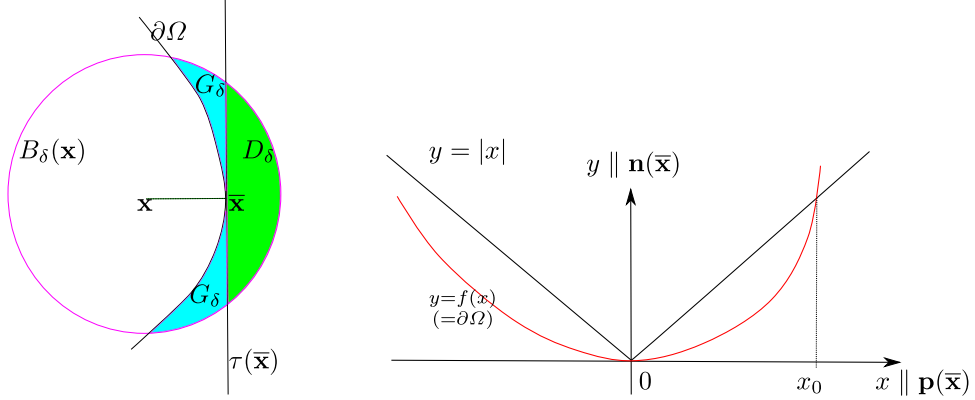


Fig. 2. Notation for geometric estimates: Left: illustration of regions D_δ and G_δ . Green represents D_δ , the region in $B_\delta(\mathbf{x})$ which lies opposite the boundary tangent at $\bar{\mathbf{x}}$. Cyan represents G_δ , the region in $B_\delta(\mathbf{x})$ which lies between $\partial\Omega$ and the boundary tangent. Right: Local Cartesian coordinate system in neighborhood of $\bar{\mathbf{x}}$. Here, the region G_δ lies below the red curve $y = f(x)$ when $\mathbf{x} = \bar{\mathbf{x}}$. (For interpretation of the references to color in this figure legend, the reader is referred to the web version of this article.)

We estimate first the D_δ part. Rewriting $\mathbf{y} \in D_\delta$ as $\mathbf{x} + (r \cos(\theta), r \sin(\theta))$ with $s_x < r < \delta$ and $-\pi/2 \leq -\arccos(s_x/r) \leq \theta \leq \arccos(s_x/r) \leq \pi/2$, we obtain

$$\begin{aligned} \int_{D_\delta} K((\mathbf{y} - \mathbf{x}) \cdot \mathbf{p})^2 d\mathbf{y} &= \int_{s_x}^{\delta} \int_{-\arccos(s_x/r)}^{\arccos(s_x/r)} K(r)r^3 \sin^2 \theta d\theta dr \leq \int_0^{\delta} \int_{-\pi/2}^{\pi/2} K(r)r^3 \sin^2 \theta d\theta dr = m(\delta)/4, \\ \int_{D_\delta} K((\mathbf{y} - \mathbf{x}) \cdot \mathbf{n})^2 d\mathbf{y} &= \int_{s_x}^{\delta} \int_{-\arccos(s_x/r)}^{\arccos(s_x/r)} K(r)r^3 \cos^2 \theta d\theta dr \leq \int_0^{\delta} \int_{-\pi/2}^{\pi/2} K(r)r^3 \cos^2 \theta d\theta dr = m(\delta)/4, \\ \int_{D_\delta} K((\mathbf{y} - \mathbf{x}) \cdot \mathbf{p})((\mathbf{y} - \mathbf{x}) \cdot \mathbf{n}) d\mathbf{y} &= 0, \end{aligned}$$

since the first two terms decrease monotonically with increasing s_x . We then have

$$\frac{d}{m(\delta)} \begin{bmatrix} \int_{D_\delta} K((\mathbf{y} - \mathbf{x}) \cdot \mathbf{p})^2 d\mathbf{y} & \int_{D_\delta} K((\mathbf{y} - \mathbf{x}) \cdot \mathbf{p})((\mathbf{y} - \mathbf{x}) \cdot \mathbf{n}) d\mathbf{y} \\ \int_{D_\delta} K((\mathbf{y} - \mathbf{x}) \cdot \mathbf{p})((\mathbf{y} - \mathbf{x}) \cdot \mathbf{n}) d\mathbf{y} & \int_{D_\delta} K((\mathbf{y} - \mathbf{x}) \cdot \mathbf{n})^2 d\mathbf{y} \end{bmatrix} = \begin{bmatrix} d_p & 0 \\ 0 & d_n \end{bmatrix}$$

where $0 \leq d_p, d_n \leq 1/2$. We now proceed to show that for a domain with C^3 regularity, the magnitude of all elements in the matrix

$$\frac{d}{m(\delta)} \begin{bmatrix} \int_{G_\delta} K((\mathbf{y} - \mathbf{x}) \cdot \mathbf{p})^2 d\mathbf{y} & \int_{G_\delta} K((\mathbf{y} - \mathbf{x}) \cdot \mathbf{p})((\mathbf{y} - \mathbf{x}) \cdot \mathbf{n}) d\mathbf{y} \\ \int_{G_\delta} K((\mathbf{y} - \mathbf{x}) \cdot \mathbf{p})((\mathbf{y} - \mathbf{x}) \cdot \mathbf{n}) d\mathbf{y} & \int_{G_\delta} K((\mathbf{y} - \mathbf{x}) \cdot \mathbf{n})^2 d\mathbf{y} \end{bmatrix}$$

are bounded by $O(\delta^2)$. Note that with the Cartesian coordinate system in Fig. 2, $\bar{\mathbf{x}} = (0, 0)$ and $\tau(\bar{\mathbf{x}}) = \{y = 0\}$. Let: $y = f(x)$ be the curve describing $\partial\Omega$; $\kappa(\mathbf{x})$ denote the curvature of $\partial\Omega_N$ at $\bar{\mathbf{x}}$; and $(c_1(l), c_2(l))$ be the parameterization of the boundary $\partial\Omega$ by the arclength l . Note that the range of l depends upon the particular geometry of $\partial\Omega$. Then we have $\mathbf{x}_l = (c_1(l), c_2(l))^T$, and

$$\mathbf{x}_l = \bar{\mathbf{x}} + \begin{pmatrix} l \\ 0 \end{pmatrix} + \begin{pmatrix} 0 \\ \frac{\kappa(\bar{\mathbf{x}})l^2}{2} \end{pmatrix} + \begin{pmatrix} c_1'''(0)\frac{l^3}{6} \\ c_2'''(0)\frac{l^3}{6} \end{pmatrix} + O(l^4).$$

The area $|G_\delta| \leq |\kappa(\bar{\mathbf{x}})| \frac{\delta^3}{3} + O(\delta^4)$. Therefore, when δ is sufficiently small, for the kernel K in (2.4) we have

$$\frac{d}{m(\delta)} \left| \int_{G_\delta} K((\mathbf{y} - \mathbf{x}) \cdot \mathbf{p})^2 d\mathbf{y} \right| \leq \frac{3}{\pi \delta^3} |G_\delta| \delta \leq \frac{1}{\pi} |\kappa(\bar{\mathbf{x}})| \delta + O(\delta^2) \leq O(\delta).$$

A similar bound follows for $\frac{d}{m(\delta)} \left| \int_{G_\delta} K((\mathbf{y} - \mathbf{x}) \cdot \mathbf{n})^2 d\mathbf{y} \right|$. For $\frac{d}{m(\delta)} \left| \int_{G_\delta} K((\mathbf{y} - \mathbf{x}) \cdot \mathbf{n})((\mathbf{y} - \mathbf{x}) \cdot \mathbf{p}) d\mathbf{y} \right|$, following from the symmetry of K ,

$$\frac{d}{m(\delta)} \left| \int_{G_\delta} K((\mathbf{y} - \mathbf{x}) \cdot \mathbf{p})((\mathbf{y} - \mathbf{x}) \cdot \mathbf{n}) d\mathbf{y} \right| = \frac{d}{m(\delta)} \left| \int_{E_\delta} K((\mathbf{y} - \mathbf{x}) \cdot \mathbf{p})((\mathbf{y} - \mathbf{x}) \cdot \mathbf{n}) d\mathbf{y} \right|,$$

where E_δ denotes the region in G_δ which is asymmetric with respect to the y axis in the right plot of Fig. 2. As shown in [18], the area of E_δ has $|E_\delta| \leq O(\delta^4)$. Therefore

$$\frac{d}{m(\delta)} \left| \int_{E_\delta} K((\mathbf{y} - \mathbf{x}) \cdot \mathbf{p})((\mathbf{y} - \mathbf{x}) \cdot \mathbf{n}) d\mathbf{y} \right| \leq O(\delta^2).$$

For sufficiently small δ we have

$$|\det(\mathbf{M}^{-1})| \geq (1 - d_p)(1 - d_n) - C(2 - d_p - d_n)\delta - C\delta^2 \geq \frac{1}{4} - C\delta > 0. \quad \square$$

Remark 1. From the proof of Theorem 3.1, we note that when $|E_\delta| = 0$, i.e., when $B_\delta(\mathbf{x}) \setminus \Omega$ is symmetric with respect to $\mathbf{n}(\bar{\mathbf{x}})$, then

$$\mathbf{M} = \begin{bmatrix} \left(\frac{d}{m(\delta)} \int_{B_\delta(\mathbf{x}) \cap \Omega} K((\mathbf{y} - \mathbf{x}) \cdot \mathbf{p})^2 d\mathbf{y} \right)^{-1} & 0 \\ 0 & \left(\frac{d}{m(\delta)} \int_{B_\delta(\mathbf{x}) \cap \Omega} ((\mathbf{y} - \mathbf{x}) \cdot \mathbf{n})^2 d\mathbf{y} \right)^{-1} \end{bmatrix}. \quad (3.5)$$

We now show that the nonlocal dilatation θ^{corr} is consistent with the local dilatation:

Theorem 3.2. Assume that $\mathbf{u} \in C^1$ and Ω is a C^3 domain, then there exists $\bar{\delta} > 0$ such that for any $0 < \delta \leq \bar{\delta}$,

$$|\theta^{corr}(\mathbf{x}) - \nabla \cdot \mathbf{u}(\mathbf{x})| = O(\delta)$$

for $\mathbf{x} \in \mathcal{I}\Omega_N$. If \mathbf{u} further satisfies $\mathbf{u} \in C^2$, then

$$|\theta^{corr}(\mathbf{x}) - \nabla \cdot \mathbf{u}(\mathbf{x})| = O(\delta^2) + O(\delta)|\mathbf{u}|_{2,\infty},$$

where $|\mathbf{u}|_{2,\infty}$ is the Sobolev seminorm representing the maximum of the Hessian matrix elements for each component of \mathbf{u} .

Proof. We again adopt the coordinate system from Fig. 2. Denoting u_p, u_n as the displacement components along the directions of $\mathbf{p}(\bar{\mathbf{x}})$ and $\mathbf{n}(\bar{\mathbf{x}})$, respectively, for $\mathbf{u} \in C^2$ we have

$$\begin{aligned} & \theta^{corr} - \nabla \cdot \mathbf{u} \\ &= \frac{d}{m(\delta)} \left(M_{11} \int_{B_\delta(\mathbf{x}) \cap \Omega} K((\mathbf{y} - \mathbf{x}) \cdot \mathbf{p})(u_p(\mathbf{y}) - u_p(\mathbf{x})) d\mathbf{y} + M_{22} \int_{B_\delta(\mathbf{x}) \cap \Omega} K((\mathbf{y} - \mathbf{x}) \cdot \mathbf{n})(u_n(\mathbf{y}) - u_n(\mathbf{x})) d\mathbf{y} \right. \\ & \quad \left. + M_{12} \int_{B_\delta(\mathbf{x}) \cap \Omega} K((\mathbf{y} - \mathbf{x}) \cdot \mathbf{p})(u_n(\mathbf{y}) - u_n(\mathbf{x})) + K((\mathbf{y} - \mathbf{x}) \cdot \mathbf{n})(u_p(\mathbf{y}) - u_p(\mathbf{x})) d\mathbf{y} \right) - \frac{\partial u_p}{\partial \mathbf{p}}(\mathbf{x}) - \frac{\partial u_n}{\partial \mathbf{n}}(\mathbf{x}) \\ &= \frac{d}{m(\delta)} \left(M_{11} \frac{\partial u_p}{\partial \mathbf{p}}(\mathbf{x}) \int_{B_\delta(\mathbf{x}) \cap \Omega} K|(\mathbf{y} - \mathbf{x}) \cdot \mathbf{p}|^2 d\mathbf{y} + M_{22} \frac{\partial u_n}{\partial \mathbf{n}}(\mathbf{x}) \int_{B_\delta(\mathbf{x}) \cap \Omega} K|(\mathbf{y} - \mathbf{x}) \cdot \mathbf{n}|^2 d\mathbf{y} \right. \\ & \quad \left. + M_{11}[u_p(\mathbf{x})]_{np} \int_{B_\delta(\mathbf{x}) \cap \Omega} K[(\mathbf{y} - \mathbf{x}) \cdot \mathbf{p}]^2 [(\mathbf{y} - \mathbf{x}) \cdot \mathbf{n}] d\mathbf{y} \right. \\ & \quad \left. + M_{22} \int_{B_\delta(\mathbf{x}) \cap \Omega} K[(\mathbf{y} - \mathbf{x}) \cdot \mathbf{n}] ([u_n(\mathbf{x})]_{nn} [(\mathbf{y} - \mathbf{x}) \cdot \mathbf{n}]^2 + [u_n(\mathbf{x})]_{pp} [(\mathbf{y} - \mathbf{x}) \cdot \mathbf{p}]^2) d\mathbf{y} \right. \\ & \quad \left. + M_{12} \left(\frac{\partial u_p}{\partial \mathbf{n}} + \frac{\partial u_n}{\partial \mathbf{p}} \right) \int_{E_\delta} K((\mathbf{y} - \mathbf{x}) \cdot \mathbf{p})((\mathbf{y} - \mathbf{x}) \cdot \mathbf{n}) d\mathbf{y} + O(\delta^5) \right) - \frac{\partial u_p}{\partial \mathbf{p}}(\mathbf{x}) - \frac{\partial u_n}{\partial \mathbf{n}}(\mathbf{x}) \\ &= O(\delta^2) + A_1(\mathbf{x})[u_p(\mathbf{x})]_{np} + A_2(\mathbf{x})[u_n(\mathbf{x})]_{nn} + A_3(\mathbf{x})[u_n(\mathbf{x})]_{pp} = O(\delta), \end{aligned} \quad (3.6)$$

where

$$A_1(\mathbf{x}) := \frac{\int_{B_\delta(\mathbf{x}) \cap \Omega} K(|\mathbf{y} - \mathbf{x}|) [(\mathbf{y} - \mathbf{x}) \cdot \mathbf{p}]^2 [(\mathbf{y} - \mathbf{x}) \cdot \mathbf{n}] d\mathbf{y}}{\int_{B_\delta(\mathbf{x}) \cap \Omega} K[(\mathbf{y} - \mathbf{x}) \cdot \mathbf{p}]^2 d\mathbf{y}},$$

$$A_2(\mathbf{x}) := \frac{\int_{B_\delta(\mathbf{x}) \cap \Omega} K(|\mathbf{y} - \mathbf{x}|) [(\mathbf{y} - \mathbf{x}) \cdot \mathbf{n}]^3 d\mathbf{y}}{2 \int_{B_\delta(\mathbf{x}) \cap \Omega} K[(\mathbf{y} - \mathbf{x}) \cdot \mathbf{n}]^2 d\mathbf{y}},$$

$$A_3(\mathbf{x}) := \frac{\int_{B_\delta(\mathbf{x}) \cap \Omega} K(|\mathbf{y} - \mathbf{x}|) [(\mathbf{y} - \mathbf{x}) \cdot \mathbf{p}]^2 [(\mathbf{y} - \mathbf{x}) \cdot \mathbf{n}] d\mathbf{y}}{2 \int_{B_\delta(\mathbf{x}) \cap \Omega} K[(\mathbf{y} - \mathbf{x}) \cdot \mathbf{n}]^2 d\mathbf{y}}.$$

For $\mathbf{u} \in C^1$, the conclusion can be shown with Taylor expansion following a similar procedure as above. \square

Having proven well-posedness and accuracy of the nonlocal dilatation, we next show that the formulation in (3.4) approximately passes the linear patch test in the local limit.

Theorem 3.3. Given that $\Omega \in \mathbb{R}^d$ ($d = 2$) is a C^3 domain, and a linear displacement field \mathbf{u} which is a solution of the classical linear elastic problem in the absence of forcing term \mathbf{f} :

$$\begin{cases} -\nabla \cdot (\lambda \text{tr}(\mathbf{E}) \mathbf{I} + 2\mu \mathbf{E}) = 0, & \text{where } \mathbf{E} = \frac{1}{2}(\nabla \mathbf{u} + (\nabla \mathbf{u})^T), \quad \text{in } \Omega, \\ \lambda \text{tr}(\mathbf{E}) \mathbf{n} + 2\mu \mathbf{E} \mathbf{n} = \mathbf{T}, & \text{on } \partial \Omega_N, \\ \mathbf{u} = \mathbf{u}_D, & \text{on } \mathcal{B}\mathcal{B}\Omega_D. \end{cases}$$

When $|E_\delta| = 0$, i.e., $B_\delta(\mathbf{x}) \setminus \Omega$ is symmetric with respect to $\mathbf{n}(\bar{\mathbf{x}})$ for all $\mathbf{x} \in \mathcal{I}\Omega_N$, \mathbf{u} is also the solution of the state-based peridynamic problem (3.4) in the absence of forcing term \mathbf{f} . When $B_\delta(\mathbf{x}) \setminus \Omega$ is not symmetric, \mathbf{u} passes the linear patch test approximately in $\mathcal{I}\Omega_N$, i.e., $\mathcal{L}_\delta \mathbf{u}(\mathbf{x}) = \mathbf{f}(\mathbf{x})$ for $\mathbf{x} \in \Omega \setminus \mathcal{I}\Omega_N$, and $\mathcal{L}_{N\delta} \mathbf{u}(\mathbf{x}) = \mathbf{f}_{N\delta}(\mathbf{x}) + O(\delta)\mathbf{1}$ for $\mathbf{x} \in \mathcal{I}\Omega_N$.

Proof. Taking a linear displacement field $\mathbf{u} = \mathbb{D}\mathbf{x} + \mathbf{b}$ where $\mathbb{D} \in \mathbb{R}^{d \times d}$, $\mathbf{b} \in \mathbb{R}^d$, for $\mathbf{x} \in \Omega \setminus \mathcal{I}\Omega_N$ the proof can be found in, e.g., [51]. We therefore focus on $\mathbf{x} \in \mathcal{I}\Omega_N$, and again employ the notation in Fig. 2. Moreover, we denote the elements of \mathbb{D} as D_{ij} , $i, j \in \{1, 2\}$.

We first consider the case when $|E_\delta| = 0$ for all $\mathbf{x} \in \mathcal{I}\Omega_N$. Substituting (3.5) into the definition of θ in (3.4), we obtain $\theta(\mathbf{x}) = D_{11} + D_{22}$ for all $\mathbf{x} \in \Omega \cup \mathcal{B}\Omega_D$. Note that

$$T_p = \mu \left(\frac{\partial u_p}{\partial \mathbf{n}} + \frac{\partial u_n}{\partial \mathbf{p}} \right) = \mu(D_{12} + D_{21}), \quad T_n = \lambda \nabla \cdot \mathbf{u} + 2\mu \frac{\partial u_n}{\partial \mathbf{n}} = (\lambda + 2\mu)D_{22} + \lambda D_{11},$$

the proof of $\mathcal{L}_{N\delta}\mathbf{u}(\mathbf{x}) = \mathbf{f}_{N\delta}(\mathbf{x})$ is obtained via a straightforward substitution of \mathbf{u} and θ into (3.3).

We now consider the general case. Combining $\mathbf{u} = \mathbb{D}\mathbf{x} + \mathbf{b}$ and (3.6) yields $\theta(\mathbf{x}) = D_{11} + D_{22} + O(\delta^2)$. Substituting the definitions of θ and \mathbf{u} into (3.3), we then have:

$$\begin{aligned}
& \mathcal{L}_{N\delta} \mathbf{u}(\mathbf{x}) - \mathbf{f}_{N\delta}(\mathbf{x}) \\
&= O(\delta) \mathbf{1} - \frac{2C_\alpha(D_{11} + D_{22})}{m(\delta)} \int_{B_\delta(\mathbf{x})} (\lambda - \mu) K(\mathbf{y} - \mathbf{x}) d\mathbf{y} \\
&\quad - \frac{C_\beta}{m(\delta)} \int_{B_\delta(\mathbf{x}) \cap \Omega} \mu K \frac{(\mathbf{y} - \mathbf{x}) \otimes (\mathbf{y} - \mathbf{x})}{|\mathbf{y} - \mathbf{x}|^2} \cdot \mathbb{D}(\mathbf{y} - \mathbf{x}) d\mathbf{y} \\
&\quad - \frac{C_\beta(D_{11} + D_{22})}{2m(\delta)} \int_{B_\delta(\mathbf{x}) \setminus \Omega} (\lambda + 2\mu) K \frac{[(\mathbf{y} - \mathbf{x}) \cdot \mathbf{n}] [(\mathbf{y} - \mathbf{x}) \cdot \mathbf{p}]^2}{|\mathbf{y} - \mathbf{x}|^2} \mathbf{n} d\mathbf{y} \\
&\quad + \frac{C_\beta(D_{11} + D_{22})}{2m(\delta)} \int_{B_\delta(\mathbf{x}) \setminus \Omega} \lambda K \frac{[(\mathbf{y} - \mathbf{x}) \cdot \mathbf{n}]^3}{|\mathbf{y} - \mathbf{x}|^2} \mathbf{n} d\mathbf{y} \\
&\quad - \frac{C_\beta \mu (D_{12} + D_{21})}{m(\delta)} \int_{B_\delta(\mathbf{x}) \setminus \Omega} K \frac{[(\mathbf{y} - \mathbf{x}) \cdot \mathbf{n}]}{|\mathbf{y} - \mathbf{x}|^2} [(\mathbf{y} - \mathbf{x}) \cdot \mathbf{p}]^2 \mathbf{p} d\mathbf{y} \\
&\quad - \frac{C_\beta [(\lambda + 2\mu) D_{22} + \lambda D_{11}]}{2m(\delta)} \int_{B_\delta(\mathbf{x}) \setminus \Omega} K \frac{[(\mathbf{y} - \mathbf{x}) \cdot \mathbf{n}]}{|\mathbf{y} - \mathbf{x}|^2} \left([(\mathbf{y} - \mathbf{x}) \cdot \mathbf{n}]^2 - [(\mathbf{y} - \mathbf{x}) \cdot \mathbf{p}]^2 \right) \mathbf{n} d\mathbf{y}
\end{aligned}$$

$$\begin{aligned}
&= \frac{C_\beta}{m(\delta)} \int_{E_\delta} \mu K \frac{D_{11}[(\mathbf{y} - \mathbf{x}) \cdot \mathbf{p}]^3 + D_{22}[(\mathbf{y} - \mathbf{x}) \cdot \mathbf{p}][(\mathbf{y} - \mathbf{x}) \cdot \mathbf{n}]^2}{|\mathbf{y} - \mathbf{x}|^2} \mathbf{p} d\mathbf{y} \\
&+ \frac{C_\beta}{m(\delta)} \int_{E_\delta} \mu K \frac{(D_{12} + D_{21})[(\mathbf{y} - \mathbf{x}) \cdot \mathbf{p}][(\mathbf{y} - \mathbf{x}) \cdot \mathbf{n}]^2}{|\mathbf{y} - \mathbf{x}|^2} \mathbf{n} d\mathbf{y} + O(\delta) \mathbf{1}. \quad \square
\end{aligned}$$

Corollary 1. Given that $\Omega \in \mathbb{R}^d$ ($d = 2$) is a C^3 domain and $|E_\delta| = 0$, then the set of rigid deformations Π is in the solution set of (3.4) with $\mathbf{f} = 0$ and $\mathbf{T} = 0$.

We now investigate the consistency of the proposed mixed-type volume constraint formulation for general \mathbf{u} , by considering the truncation estimate of the local solution. We denote \mathbf{u}_δ as the solution of the nonlocal problem (3.4) and \mathbf{u}_0 as the solution of the corresponding linear elasticity problem:

$$\begin{cases} \mathcal{L}_0 \mathbf{u} = -\nabla \cdot (\lambda \text{tr}(\mathbf{E}) \mathbf{I} + 2\mu \mathbf{E}) = \mathbf{f}, & \text{where } \mathbf{E} = \frac{1}{2}(\nabla \mathbf{u} + (\nabla \mathbf{u})^T), \quad \text{in } \Omega, \\ \lambda \text{tr}(\mathbf{E}) \mathbf{n} + 2\mu \mathbf{E} \mathbf{n} = \mathbf{T}, & \text{on } \partial \Omega_N, \\ \mathbf{u} = \mathbf{u}_D, & \text{on } \mathcal{B}\mathcal{B}\Omega_D. \end{cases} \quad (3.7)$$

Denoting the truncation estimate $\mathbf{e}_\delta(\mathbf{x}) := \mathcal{L}_\delta \mathbf{u}_\delta(\mathbf{x}) - \mathcal{L}_\delta \mathbf{u}_0(\mathbf{x})$ for $\mathbf{x} \in \Omega \setminus \mathcal{I}\Omega_N$ and $\mathbf{e}_\delta(\mathbf{x}) := \mathcal{L}_{N\delta} \mathbf{u}_\delta(\mathbf{x}) - \mathcal{L}_{N\delta} \mathbf{u}_0(\mathbf{x})$ for $\mathbf{x} \in \mathcal{I}\Omega_N$, we may obtain the following bound for \mathbf{e}_δ :

Theorem 3.4. Assume that the local solution $\mathbf{u}_0 \in C^1$, then $|\mathbf{e}_\delta| = O(\delta^2)$ for $\mathbf{x} \in \Omega \setminus \mathcal{I}\Omega_N$ and $|\mathbf{e}_\delta| = O(1)$ for $\mathbf{x} \in \mathcal{I}\Omega_N$.

Proof. For $\mathbf{x} \in \Omega \setminus \mathcal{I}\Omega_N$, from $\mathbf{e}_\delta = \mathbf{f}(\mathbf{x}) - \mathcal{L}_\delta \mathbf{u}_0(\mathbf{x}) = \mathcal{L}_0 \mathbf{u}_0(\mathbf{x}) - \mathcal{L}_\delta \mathbf{u}_0(\mathbf{x})$, the bound of \mathbf{e}_δ may be obtained via Taylor expansion of \mathbf{u}_0 following a similar derivation as in [18]. Denoting u_{0p} , u_{0n} as the components of \mathbf{u}_0 along the tangential and normal directions, respectively, for $\mathbf{x} \in \mathcal{I}\Omega_N$, with the calculation in (3.6) we have $\theta(\mathbf{u}_0) - \nabla \cdot \mathbf{u}_0 = O(\delta)$. Note that the tangential and normal components of the traction load satisfies

$$T_p = \mu \left(\frac{\partial u_{0p}}{\partial \mathbf{n}} + \frac{\partial u_{0n}}{\partial \mathbf{p}} \right), \quad T_n = \lambda \nabla \cdot \mathbf{u}_0 + 2\mu \frac{\partial u_{0n}}{\partial \mathbf{n}},$$

and with the Taylor expansion of \mathbf{u}_0 , for $\mathbf{x} \in \mathcal{I}\Omega_N$ we have

$$\begin{aligned}
\mathbf{e}_\delta &= (\mathcal{L}_0 \mathbf{u}_0 - \mathcal{L}_{N\delta} \mathbf{u}_0) + (\mathbf{f}_{N\delta} - \mathbf{f}) = -\frac{1}{2} \nabla \cdot (\lambda \text{tr}(\nabla \mathbf{u}_0 + (\nabla \mathbf{u}_0)^T) \mathbf{I} + 2\mu(\nabla \mathbf{u}_0 + (\nabla \mathbf{u}_0)^T)) \\
&+ \frac{C_\alpha(\lambda - \mu)}{m(\delta)} \int_{B_\delta(\mathbf{x}) \cap \Omega} K(\mathbf{y} - \mathbf{x})(\nabla \cdot \mathbf{u}_0(\mathbf{x}) + \nabla \cdot \mathbf{u}_0(\mathbf{y})) d\mathbf{y} \\
&+ \frac{C_\beta}{m(\delta)} \int_{B_\delta(\mathbf{x}) \cap \Omega} \mu K \frac{(\mathbf{y} - \mathbf{x}) \otimes (\mathbf{y} - \mathbf{x})}{|\mathbf{y} - \mathbf{x}|^2} (\mathbf{u}_0(\mathbf{y}) - \mathbf{u}_0(\mathbf{x})) d\mathbf{y} + \frac{2C_\alpha \nabla \cdot \mathbf{u}_0(\mathbf{x})}{m(\delta)} \int_{B_\delta(\mathbf{x}) \setminus \Omega} (\lambda - \mu) K(\mathbf{y} - \mathbf{x}) d\mathbf{y} \\
&+ \frac{C_\beta \nabla \cdot \mathbf{u}_0(\mathbf{x})}{2m(\delta)} \int_{B_\delta(\mathbf{x}) \setminus \Omega} (\lambda + 2\mu) K \frac{[(\mathbf{y} - \mathbf{x}) \cdot \mathbf{n}][(\mathbf{y} - \mathbf{x}) \cdot \mathbf{p}]^2}{|\mathbf{y} - \mathbf{x}|^2} \mathbf{n} d\mathbf{y} \\
&- \frac{C_\beta \nabla \cdot \mathbf{u}_0(\mathbf{x})}{2m(\delta)} \int_{B_\delta(\mathbf{x}) \setminus \Omega} \lambda K \frac{[(\mathbf{y} - \mathbf{x}) \cdot \mathbf{n}]^3}{|\mathbf{y} - \mathbf{x}|^2} \mathbf{n} d\mathbf{y} + \frac{C_\beta}{m(\delta)} \int_{B_\delta(\mathbf{x}) \setminus \Omega} K \frac{[(\mathbf{y} - \mathbf{x}) \cdot \mathbf{n}]}{|\mathbf{y} - \mathbf{x}|^2} [(\mathbf{y} - \mathbf{x}) \cdot \mathbf{p}]^2 [T_p(\bar{\mathbf{x}}) \mathbf{p}] d\mathbf{y} \\
&+ \frac{C_\beta}{2m(\delta)} \int_{B_\delta(\mathbf{x}) \setminus \Omega} K \frac{[(\mathbf{y} - \mathbf{x}) \cdot \mathbf{n}]}{|\mathbf{y} - \mathbf{x}|^2} \left([(\mathbf{y} - \mathbf{x}) \cdot \mathbf{n}]^2 - [(\mathbf{y} - \mathbf{x}) \cdot \mathbf{p}]^2 \right) [T_n(\bar{\mathbf{x}}) \mathbf{n}] d\mathbf{y} + \mathcal{O}(1) \mathbf{1} = \mathcal{O}(1) \mathbf{1}. \quad \square
\end{aligned}$$

Remark 2. From Theorem 4.2 in the next section, we will see that given the possible numerical error from boundary approximations in the meshfree formulation, the $O(1)$ truncation estimate of \mathbf{e}_δ for $\mathbf{x} \in \mathcal{I}\Omega_N$ is of optimal in M-convergence tests.

Remark 3. To theoretically show the L^2 convergence of \mathbf{u}_δ to the local limit \mathbf{u}_0 , a nonlocal Poincaré–Korn’s inequality would be required which will be addressed in the future work. In this work we demonstrate the asymptotic convergence rate with numerical examples in Section 5, where a first order convergence $O(\delta)$ is observed for $\|\mathbf{u}_\delta - \mathbf{u}_0\|_{L^2(\Omega)}$, which indicates that the $O(1)$ truncation estimate in $\mathcal{I}\Omega_N$ is sufficient to obtain asymptotic

convergence when $\delta = O(h)$. A similar phenomenon was also observed on the Neumann constraint nonlocal diffusion problem in [18].

4. Optimization-based meshfree quadrature rules

In this section, we introduce a strong-form particle discretization of the state-based peridynamics introduced above. Discretizing the whole interaction region $\Omega \cup \mathcal{B}\mathcal{B}\Omega$ by a collection of points $X_h = \{\mathbf{x}_i\}_{i=1,2,\dots,N_p} \subset \Omega \cup \mathcal{B}\mathcal{B}\Omega$, we aim to solve for the displacement $\mathbf{u}_i \approx \mathbf{u}(\mathbf{x}_i)$ and the nonlocal dilatation $\theta_i \approx \theta(\mathbf{x}_i)$ on all $\mathbf{x}_i \in X_h$. We first characterize the distribution of collocation points as follows. Recall the definitions [52] of *fill distance*

$$h_{\chi_h, \Omega} = \sup_{\mathbf{u}_i \in \Omega \cup \mathcal{B}\mathcal{B}\Omega} \min_{\mathbf{x}_i \in \chi_h} \|\mathbf{x}_i - \mathbf{x}_j\|_2,$$

and *separation distance*

$$q_{\chi_h} = \frac{1}{2} \min_{i \neq j} \|\mathbf{x}_i - \mathbf{x}_j\|_2.$$

For simplicity we drop subscripts and simply write h and q . We assume that χ_h is *quasi-uniform*, namely that there exists $c_{qu} > 0$ such that

$$q_{\chi_h} \leq h_{\chi_h, \Omega} \leq c_{qu} q_{\chi_h}.$$

To maintain an easily scalable implementation, in this paper we assume δ to be chosen such that the ratio $\frac{h}{\delta}$ is bound by a constant M as $\delta \rightarrow 0$, restricting ourselves to the “M-convergence” scenario [23].

As the first step, for the original LPS model (2.1), we pursue a discretization through the following one point quadrature rule at a collection of collocation points X_h [53]:

$$\begin{aligned} (\mathcal{L}_\delta^h \mathbf{u})_i &:= -\frac{C_\alpha}{m(\delta)} \sum_{\mathbf{x}_j \in B_\delta(\mathbf{x}_i)} (\lambda - \mu) K_{ij} (\mathbf{x}_j - \mathbf{x}_i) (\theta_i + \theta_j) \omega_{j,i} \\ &\quad - \frac{C_\beta}{m(\delta)} \sum_{\mathbf{x}_j \in B_\delta(\mathbf{x}_i)} \mu K_{ij} \frac{(\mathbf{x}_j - \mathbf{x}_i) \otimes (\mathbf{x}_j - \mathbf{x}_i)}{|\mathbf{x}_j - \mathbf{x}_i|^2} \cdot (\mathbf{u}_j - \mathbf{u}_i) \omega_{j,i} = \mathbf{f}_i, \end{aligned} \quad (4.1)$$

$$\theta(\mathbf{x}) = \frac{d}{m(\delta)} \sum_{\mathbf{x}_j \in B_\delta(\mathbf{x}_i)} K_{ij} (\mathbf{x}_j - \mathbf{x}_i) \cdot (\mathbf{u}_j - \mathbf{u}_i) \omega_{j,i}, \quad (4.2)$$

where we adapt the notations $f(\mathbf{x}_i) = f_i$ and $f(\mathbf{x}_i, \mathbf{x}_j) = f_{ij}$, and we specify $\{\omega_{j,i}\}$ as a to-be-determined collection of quadrature weights admitting interpretation as a measure associated with each collocation point \mathbf{x}_i . We define in this section an optimization-based approach to defining these weights extending previous work [17], constructed to ensure consistency guarantees. Specifically, we seek quadrature weights for integrals supported on balls of the form

$$I[f] := \int_{B_\delta(\mathbf{x}_i)} f(\mathbf{x}, \mathbf{y}) d\mathbf{y} \approx I_h[f] := \sum_{\mathbf{x}_j \in B_\delta(\mathbf{x}_i)} f(\mathbf{x}_i, \mathbf{x}_j) \omega_{j,i} \quad (4.3)$$

where we include the subscript i in $\{\omega_{j,i}\}$ to denote that we seek a different family of quadrature weights for different subdomains $B_\delta(\mathbf{x}_i)$. We obtain these weights from the following optimization problem

$$\operatorname{argmin}_{\{\omega_{j,i}\}} \sum_{\mathbf{x}_j \in B_\delta(\mathbf{x}_i)} \omega_{j,i}^2 \quad \text{such that,} \quad I_h[p] = I[p] \quad \forall p \in \mathbf{V}_h \quad (4.4)$$

where \mathbf{V}_h denotes a Banach space of functions which should be integrated exactly. We refer to previous work [17] for further information, analysis, and implementation details.

Provided the quadrature points are unisolvant over the desired reproducing space, this problem may be proven to have a solution by interpreting it as a generalized moving least squares (GMLS) problem [12]. For certain choices of \mathbf{V}_h , such as m th-order polynomials, unisolvency holds under the assumptions that: the domain Ω satisfies a cone condition, the pointset $X_h \cap B_\delta(\mathbf{x}_i)$ is quasi-uniform, and δ is sufficiently large [52].

In previous work we have provided truncation error estimates relating the quadrature error convergence rate to the order of singularity in the kernel. As discussed in [17], the key to obtaining these quadrature weights is that they may be evaluated analytically, either via analytic rules [54] or the aid of symbolic integration software. In this work, we choose a reproducing space sufficient to integrate (4.1) and (4.2) exactly in the case where \mathbf{u} and θ are quadratic polynomials.

Theorem 4.1. *Let $\mathbf{V}_h = \left\{ q = \frac{p(\mathbf{y})}{|\mathbf{y}-\mathbf{x}|^3} \mid p \in P_5(\mathbb{R}^d) \text{ such that } \int_{B_\delta(\mathbf{x})} q(\mathbf{y}) d\mathbf{y} < \infty \right\}$ where $p \in P_5(\mathbb{R}^d)$ is the space of quintic polynomials, and assume $B_\delta(\mathbf{x}) \subset \Omega \cup \mathcal{BB}\Omega_D$ and that the optimization problem (4.4) has a solution. Then the meshfree optimization-based quadrature (OBQ) approximations to (2.1) and (2.2) are exact for $\mathbf{u} \in (P_3(\mathbb{R}^d))^d$ and $\theta \in P_2(\mathbb{R}^d)$. Further, for $\mathbf{u} \in C^3$ and $\theta \in C^2$ the truncation error for all nonlocal operators in (2.1) converge to its local limit with an $O(\delta^2)$ rate in the limit $\delta \rightarrow 0$.*

Proof. We prove only for the nonlocal gradient; the other operators follow similarly. Rewriting the gradient as $\int_{B_\delta(\mathbf{x})} \frac{|\mathbf{x}-\mathbf{y}|^2}{|\mathbf{x}-\mathbf{y}|^3} (\mathbf{y}-\mathbf{x}) (\theta(\mathbf{x}) + \theta(\mathbf{y})) d\mathbf{y}$ and assuming $\theta \in P_2$, we obtain a component-wise form $\int_{B_\delta(\mathbf{x})} \frac{p(\mathbf{y})}{|\mathbf{x}-\mathbf{y}|^3} d\mathbf{y}$ where $p \in P_5$, and thus the quadrature is exact via the equality constraint of (4.4). To prove convergence, note that we may rewrite $\int_{B_\delta(\mathbf{x})} \frac{|\mathbf{x}-\mathbf{y}|^2}{|\mathbf{x}-\mathbf{y}|^3} (\mathbf{y}-\mathbf{x}) (\theta(\mathbf{y}) - \theta(\mathbf{x})) d\mathbf{y}$ because constants are in the null-space of the nonlocal gradient. The proof then follows from Thm. 2.1 of [17], by approximating $\theta(\mathbf{y}) - \theta(\mathbf{x})$ via a third order Taylor series, converting to polar coordinates, and bounding terms. \square

Remark 4. We have selected this particular choice of reproducing space so that the same quadrature weights may be used for all nonlocal operators. The cost of constructing the quadrature scales as $\dim(\mathbf{V}_h)^3$, and significant savings may result by instead generating quadrature rules for each operator specifically. For example, one may obtain the same convergence by selecting $\mathbf{V}_h = \left\{ \frac{\mathbf{y}-\mathbf{x}}{|\mathbf{y}-\mathbf{x}|} (p(\mathbf{y}) + p(\mathbf{x})) \mid p \in P_2(\mathbb{R}^d) \right\}$ in the nonlocal gradient. As solving (4.4) amounts to inverting a small dense matrix, we may expect a substantial $(\dim(P_2)/\dim(P_5))^3$ speed-up in this case ($7^3 \times$ speedup in 2D and $(56/10)^3 \times$ speedup in 3D). Because the requisite optimization problems are amenable to fine-grained parallelism on GPUs using libraries such as the Compadre toolkit [55], we prefer in this work to use a single quadrature rule for all operators; in our implementation the cost of constructing the quadrature weights is negligible compared to solving the resultant stiffness matrix after discretization.

Remark 5. In many quadrature schemes it is desirable to enforce the positivity of quadrature weights (i.e. $\omega_{j,i} > 0$). While we do not pursue this property in the current work, (4.4) may be modified to enforce this property via an inequality constraint. In the context of maximum principle preserving meshfree discretizations this has been considered [56]. We note that for quasi-uniform particle distributions, we have seen only a small number of negative quadrature weights, and that these are generally very small compared to the other positive weights.

We now apply the above quadrature rule to the LPS model with traction loads applied on a sharp boundary $\partial\Omega_N$. For $\mathbf{x}_i \in \mathcal{I}\Omega_N$, we note that $B_\delta(\mathbf{x}_i) \cap \Omega \neq \emptyset$. In the meshfree formulation, the boundary $\partial\Omega_N$ is represented by breaking bonds between \mathbf{x}_i and $\mathbf{x}_j \in B_\delta(\mathbf{x}_i) \setminus \Omega$, as demonstrated in Fig. 3. For $\mathbf{x}_j \in \Omega$, we denote the bond between \mathbf{x}_i and \mathbf{x}_j as “intact” and the change of displacement on material point \mathbf{x}_j may have an impact on the displacement at \mathbf{x}_i . On the other hand, when $\mathbf{x}_j \notin \Omega$, we consider the bonds between \mathbf{x}_i and \mathbf{x}_j as “broken”. To discretize (3.1) and (3.3), the quadrature weights associated with intact bonds will be employed in the calculation of integrals inside $B_\delta(\mathbf{x}_i) \cap \Omega$ and the weights associated with broken bonds will be employed for integrals inside $B_\delta(\mathbf{x}_i) \setminus \Omega$. Particularly, we express the quadrature weights associated with intact bonds $\tilde{\omega}_{j,i}$ and the quadrature weights associated with broken bonds $\hat{\omega}_{j,i}$ in terms of the scalar mask $\gamma_{j,i}$:

$$\gamma_{j,i} = \begin{cases} 1, & \text{if } \mathbf{x}_j \in B_\delta(\mathbf{x}_i) \cap \Omega, \\ 0, & \text{otherwise,} \end{cases} \quad \tilde{\omega}_{j,i} = \omega_{j,i} \gamma_{j,i}, \quad \hat{\omega}_{j,i} = \omega_{j,i} (1 - \gamma_{j,i}). \quad (4.5)$$

Numerical quadrature of a given function $a(\mathbf{x})$ over $B_\delta(\mathbf{x}_i) \cap \Omega$ and $B_\delta(\mathbf{x}_i) \setminus \Omega$ may thus be calculated via

$$\int_{B_\delta(\mathbf{x}_i) \cap \Omega} a(\mathbf{y}) d\mathbf{y} \approx \sum_{\mathbf{x}_j \in B_\delta(\mathbf{x}_i)} \tilde{\omega}_{j,i} a(\mathbf{x}_j), \quad \int_{B_\delta(\mathbf{x}_i) \setminus \Omega} a(\mathbf{y}) d\mathbf{y} \approx \sum_{\mathbf{x}_j \in B_\delta(\mathbf{x}_i)} \hat{\omega}_{j,i} a(\mathbf{x}_j).$$

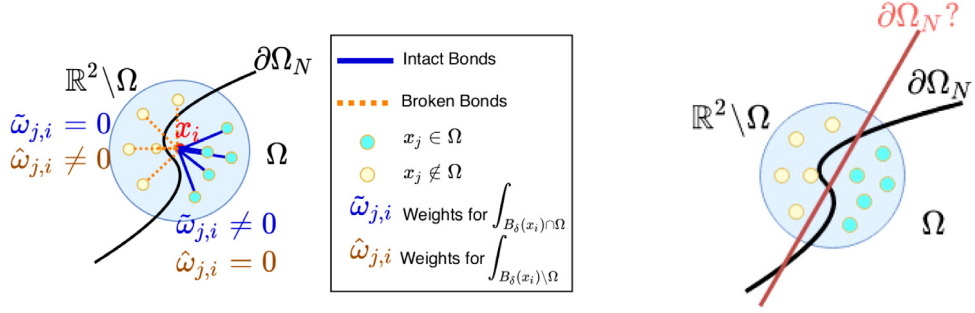


Fig. 3. Illustration of neighbor points and bonds for $\mathbf{x}_i \in \mathcal{I}\Omega_N$, where the yellow points represent $\mathbf{x}_j \notin \Omega$ and blue points represent $\mathbf{x}_j \in \Omega$. Left: An illustration of broken/intact bonds in the meshfree formulation. Right: An approximate boundary provided by breaking bonds in the meshfree formulation. The black and red curves indicate two possible boundaries represented by the same formulation in (4.6) and (4.7). With a purely volumetric particle representation of the boundary, it is not possible to avoid first order truncation estimates from errors in the representation of the geometry. (For interpretation of the references to color in this figure legend, the reader is referred to the web version of this article.)

This process is consistent with how damage is typically induced in bond-based peridynamics, such as the prototype microelastic brittle model [57]. Applying the above formulation in (3.1) and (3.3) we propose the following meshfree scheme:

$$\begin{aligned}
 (\mathcal{L}_{N\delta}^h \mathbf{u})_i &:= \sum_{\mathbf{x}_j \in B_\delta(\mathbf{x}_i)} \frac{K_{ij}}{m(\delta)} \left[\left(-C_\alpha (\lambda - \mu) (\mathbf{x}_j - \mathbf{x}_i) (\theta_i + \theta_j) - C_\beta \mu \frac{(\mathbf{x}_j - \mathbf{x}_i) \otimes (\mathbf{x}_j - \mathbf{x}_i)}{|\mathbf{x}_j - \mathbf{x}_i|^2} \cdot (\mathbf{u}_j - \mathbf{u}_i) \right) \tilde{\omega}_{j,i} \right. \\
 &\quad \left. + \left(-2C_\alpha (\lambda - \mu) (\mathbf{x}_j - \mathbf{x}_i) - \frac{C_\beta (\lambda + 2\mu) \mathbf{n}_i}{2} \frac{[(\mathbf{x}_j - \mathbf{x}_i) \cdot \mathbf{n}_i] [(\mathbf{x}_j - \mathbf{x}_i) \cdot \mathbf{p}_i]^2}{|\mathbf{x}_j - \mathbf{x}_i|^2} + \frac{C_\beta \lambda \mathbf{n}_i}{2} \frac{[(\mathbf{x}_j - \mathbf{x}_i) \cdot \mathbf{n}_i]^3}{|\mathbf{x}_j - \mathbf{x}_i|^2} \right) \theta_i \hat{\omega}_{j,i} \right] \\
 &= \mathbf{f}(\mathbf{x}_i) + \sum_{\mathbf{x}_j \in B_\delta(\mathbf{x}_i)} \frac{K_{ij} \hat{\omega}_{j,i}}{m(\delta)} \left(C_\beta T_p(\bar{\mathbf{x}}_i) \mathbf{p}_i \frac{[(\mathbf{x}_j - \mathbf{x}_i) \cdot \mathbf{n}_i]}{|\mathbf{x}_j - \mathbf{x}_i|^2} [(\mathbf{x}_j - \mathbf{x}_i) \cdot \mathbf{p}_i]^2 \right. \\
 &\quad \left. + \frac{C_\beta T_n(\bar{\mathbf{x}}_i) \mathbf{n}_i}{2} \frac{[(\mathbf{x}_j - \mathbf{x}_i) \cdot \mathbf{n}_i]}{|\mathbf{x}_j - \mathbf{x}_i|^2} \left([(\mathbf{x}_j - \mathbf{x}_i) \cdot \mathbf{n}_i]^2 - [(\mathbf{x}_j - \mathbf{x}_i) \cdot \mathbf{p}_i]^2 \right) \right) := (\mathbf{f}_{N\delta})_i, \tag{4.6}
 \end{aligned}$$

$$\theta_i = \frac{d}{m(\delta)} \sum_{\mathbf{x}_j \in B_\delta(\mathbf{x}_i)} K_{ij} (\mathbf{x}_j - \mathbf{x}_i) \cdot \mathbf{M}_i \cdot (\mathbf{u}_j - \mathbf{u}_i) \tilde{\omega}_{j,i}, \tag{4.7}$$

where

$$\mathbf{M}_i := \left[\frac{d}{m(\delta)} \sum_{\mathbf{x}_j \in B_\delta(\mathbf{x}_i)} K_{ij} (\mathbf{x}_j - \mathbf{x}_i) \otimes (\mathbf{x}_j - \mathbf{x}_i) \tilde{\omega}_{j,i} \right]^{-1}. \tag{4.8}$$

Note that although we have shown in [Theorem 3.1](#) that $\mathbf{M}(\mathbf{x}_i)$ exists when $\partial\Omega$ is sufficiently smooth, the numerical evaluation of the correction tensor further requires that $\sum_{\mathbf{x}_j \in B_\delta(\mathbf{x}_i)} K_{ij} (\mathbf{x}_j - \mathbf{x}_i) \otimes (\mathbf{x}_j - \mathbf{x}_i) \tilde{\omega}_{j,i}$ be invertible. This is true as long as there are at least d non-collinear bonds within the horizon. In some settings, such as violent dynamic fracture, for a given particle all bonds may break, leaving an isolated particle. In this case the matrix inverse \mathbf{M}_i^{-1} may be replaced with a pseudo-inverse \mathbf{M}_i^+ to improve robustness of the scheme.

Note that in the traction-type boundary condition formulation (3.3), the unit normal vector $\mathbf{n}(\bar{\mathbf{x}})$ is required, and the unit tangential vector $\mathbf{p}(\bar{\mathbf{x}})$ can then be calculated as the orthogonal unit vector of $\mathbf{n}(\bar{\mathbf{x}})$. However, in realistic settings the analytical form of $\mathbf{n}(\bar{\mathbf{x}})$ is often unavailable. To approximate the normal vector at $\bar{\mathbf{x}}_i$ for each \mathbf{x}_i , we note that

$$\mathbf{n}(\bar{\mathbf{x}}) \approx -\frac{\int_{B_\delta(\mathbf{x}) \cap \Omega} (\mathbf{y} - \mathbf{x}) d\mathbf{y}}{\left\| \int_{B_\delta(\mathbf{x}) \cap \Omega} (\mathbf{y} - \mathbf{x}) d\mathbf{y} \right\|}.$$

Therefore numerically we calculate the normal direction as \mathbf{n}_i as

$$\mathbf{n}_i = -\frac{\sum_{\mathbf{x}_j \in B_\delta(\mathbf{x}_i)} (\mathbf{x}_j - \mathbf{x}_i) \tilde{\omega}_{j,i}}{\left\| \sum_{\mathbf{x}_j \in B_\delta(\mathbf{x}_i)} (\mathbf{x}_j - \mathbf{x}_i) \tilde{\omega}_{j,i} \right\|}, \quad (4.9)$$

and the tangential vector \mathbf{p}_i is calculated as the orthogonal direction to \mathbf{n}_i .

Note that the formulation (4.9) provides a practical approximation of the unit normal vector for each $\mathbf{x} \in \mathcal{I}\Omega_N$ instead of each $\bar{\mathbf{x}} \in \partial\Omega_N$, which therefore induces possible numerical errors in (4.6). Moreover, in (4.6) and (4.7) we only solve for \mathbf{u} and θ in Ω , which is equivalent to breaking any bond intersecting the Neumann boundary $\partial\Omega_N$. We highlight that quadrature weights $\omega_{j,i}$ are computed in the reference configuration before bonds are broken, and therefore no remeshing or calculation of quadrature weights will be required as fracture progresses. This property offers an efficient and sharp treatment of boundary geometry which may be easily implemented in popular particle mechanics codes. However, as illustrated in Fig. 3, such a numerical approximation for the boundary shape $\partial\Omega_N$ introduces an $O(h)$ error to the boundary shape and correspondingly to the provided traction load \mathbf{T} on $\partial\Omega_N$, and therefore errors in (4.6) and (4.7).

To characterize the resulting numerical error, in the following we consider an equivalent problem: a perturbed traction load $\hat{\mathbf{T}}(\mathbf{x})$ is provided on $\partial\Omega_N$, i.e., there exists a constant C which is independent of h and δ , such that

$$|\hat{\mathbf{T}}(\mathbf{x}) - \mathbf{T}(\mathbf{x})| \leq Ch, \quad \forall \mathbf{x} \in \partial\Omega_N.$$

Moreover, due to the presumed perturbation of the geometry and the numerical error in (4.9), for $\mathbf{x} \in \mathcal{I}\Omega_N$ we assume that the normal and tangential directions are also perturbed such that $\hat{\mathbf{n}} - \mathbf{n} = O(h)$ and $\hat{\mathbf{p}} - \mathbf{p} = O(h)$. With the perturbed traction loads and perturbed unit vectors specified above, we denote the (perturbed) nonlocal operator defined in (3.3) as $\hat{\mathcal{L}}_{N\delta}$, the (perturbed) nonlocal dilatation defined in (3.1) as $\hat{\theta}$, and

$$\begin{aligned} \hat{\mathbf{f}}_{N\delta}(\mathbf{x}) := & \mathbf{f}(\mathbf{x}) + \frac{C_\beta}{m(\delta)} \int_{B_\delta(\mathbf{x}) \setminus \Omega} K(|\mathbf{y} - \mathbf{x}|) \frac{[(\mathbf{y} - \mathbf{x}) \cdot \hat{\mathbf{n}}]}{|\mathbf{y} - \mathbf{x}|^2} [(\mathbf{y} - \mathbf{x}) \cdot \hat{\mathbf{p}}]^2 [\hat{T}_p(\bar{\mathbf{x}}) \hat{\mathbf{p}}] d\mathbf{y} \\ & + \frac{C_\beta}{2m(\delta)} \int_{B_\delta(\mathbf{x}) \setminus \Omega} K(|\mathbf{y} - \mathbf{x}|) \frac{[(\mathbf{y} - \mathbf{x}) \cdot \hat{\mathbf{n}}]}{|\mathbf{y} - \mathbf{x}|^2} \left([(\mathbf{y} - \mathbf{x}) \cdot \hat{\mathbf{n}}]^2 - [(\mathbf{y} - \mathbf{x}) \cdot \hat{\mathbf{p}}]^2 \right) [\hat{T}_n(\bar{\mathbf{x}}) \hat{\mathbf{n}}] d\mathbf{y}. \end{aligned} \quad (4.10)$$

We then provide the truncation estimate corresponding to the above perturbations as follows.

Theorem 4.2. *Assume that $\mathbf{u} \in C^1$, Ω is C^3 smooth, $\hat{\mathbf{T}}$ is a perturbed approximation of the local traction load as defined in (3.7):*

$$\hat{T}_p(\bar{\mathbf{x}}) = \mu \left(\frac{\partial u_p}{\partial \mathbf{n}}(\mathbf{x}) + \frac{\partial u_n}{\partial \mathbf{p}}(\mathbf{x}) \right) + O(h), \quad \hat{T}_n(\bar{\mathbf{x}}) = \lambda \nabla \cdot \mathbf{u}(\mathbf{x}) + 2\mu \frac{\partial u_n}{\partial \mathbf{n}}(\mathbf{x}) + O(h), \quad \forall \mathbf{x} \in \partial\Omega_N,$$

where u_p , u_n are the components of \mathbf{u} along the non-perturbed tangential and normal directions respectively. The truncation estimates from perturbed \mathbf{T} , \mathbf{n} and \mathbf{p} for nonlocal operator in (3.3) is bounded by $O(1)$ under the M -convergence condition. Specifically,

$$|\hat{\mathcal{L}}_{N\delta} \mathbf{u} - \hat{\mathbf{f}}_{N\delta} - \mathcal{L}_{N\delta} \mathbf{u} + \mathbf{f}_{N\delta}| = O(1).$$

Proof. From the definition of nonlocal dilatation in (3.1), we note that θ is not influenced by the perturbations on traction loads and normal/tangential directions, i.e., $\hat{\theta} = \theta$. To obtain the bound for the nonlocal operator in (3.3) we separate the truncation estimate into two parts, the part from perturbation on \mathbf{T} and the part induced by the perturbation of \mathbf{n} and \mathbf{p} :

$$\hat{\mathcal{L}}_{N\delta} \mathbf{u} - \hat{\mathbf{f}}_{N\delta} - \mathcal{L}_{N\delta} \mathbf{u} + \mathbf{f}_{N\delta} = H_1 + H_2.$$

$$\begin{aligned} H_1 := & \frac{C_\beta}{m(\delta)} \int_{B_\delta(\mathbf{x}) \setminus \Omega} K \frac{[(\mathbf{y} - \mathbf{x}) \cdot \hat{\mathbf{n}}]}{|\mathbf{y} - \mathbf{x}|^2} [(\mathbf{y} - \mathbf{x}) \cdot \hat{\mathbf{p}}]^2 (T_p(\bar{\mathbf{x}}) - \hat{T}_p(\bar{\mathbf{x}})) \hat{\mathbf{p}} d\mathbf{y} \\ & + \frac{C_\beta}{2m(\delta)} \int_{B_\delta(\mathbf{x}) \setminus \Omega} K \frac{[(\mathbf{y} - \mathbf{x}) \cdot \hat{\mathbf{n}}]}{|\mathbf{y} - \mathbf{x}|^2} \left([(\mathbf{y} - \mathbf{x}) \cdot \hat{\mathbf{n}}]^2 - [(\mathbf{y} - \mathbf{x}) \cdot \hat{\mathbf{p}}]^2 \right) (T_n(\bar{\mathbf{x}}) - \hat{T}_n(\bar{\mathbf{x}})) \hat{\mathbf{n}} d\mathbf{y} \end{aligned}$$

$$\begin{aligned}
H_2 := & \frac{C_\beta(\lambda + 2\mu)\theta(\mathbf{x})}{2m(\delta)} \int_{B_\delta(\mathbf{x}) \setminus \Omega} \frac{K}{|\mathbf{y} - \mathbf{x}|^2} \left([(\mathbf{y} - \mathbf{x}) \cdot \mathbf{n}] [(\mathbf{y} - \mathbf{x}) \cdot \mathbf{p}]^2 \mathbf{n} - [(\mathbf{y} - \mathbf{x}) \cdot \hat{\mathbf{n}}] [(\mathbf{y} - \mathbf{x}) \cdot \hat{\mathbf{p}}]^2 \hat{\mathbf{n}} \right) d\mathbf{y} \\
& + \frac{C_\beta\lambda\theta(\mathbf{x})}{2m(\delta)} \int_{B_\delta(\mathbf{x}) \setminus \Omega} \frac{K}{|\mathbf{y} - \mathbf{x}|^2} \left([(\mathbf{y} - \mathbf{x}) \cdot \hat{\mathbf{n}}]^3 \hat{\mathbf{n}} - [(\mathbf{y} - \mathbf{x}) \cdot \mathbf{n}]^3 \mathbf{n} \right) d\mathbf{y} \\
& + \frac{C_\beta}{m(\delta)} \int_{B_\delta(\mathbf{x}) \setminus \Omega} \frac{K}{|\mathbf{y} - \mathbf{x}|^2} \left([(\mathbf{y} - \mathbf{x}) \cdot \mathbf{n}] [(\mathbf{y} - \mathbf{x}) \cdot \mathbf{p}]^2 [T_p(\bar{\mathbf{x}})\mathbf{p}] - [(\mathbf{y} - \mathbf{x}) \cdot \hat{\mathbf{n}}] [(\mathbf{y} - \mathbf{x}) \cdot \hat{\mathbf{p}}]^2 [T_p(\bar{\mathbf{x}})\hat{\mathbf{p}}] \right) d\mathbf{y} \\
& + \frac{C_\beta}{2m(\delta)} \int_{B_\delta(\mathbf{x}) \setminus \Omega} \frac{K}{|\mathbf{y} - \mathbf{x}|^2} \left([(\mathbf{y} - \mathbf{x}) \cdot \mathbf{n}] \left([(\mathbf{y} - \mathbf{x}) \cdot \mathbf{n}]^2 - [(\mathbf{y} - \mathbf{x}) \cdot \mathbf{p}]^2 \right) [T_n(\bar{\mathbf{x}})\mathbf{n}] \right. \\
& \quad \left. - [(\mathbf{y} - \mathbf{x}) \cdot \hat{\mathbf{n}}] \left([(\mathbf{y} - \mathbf{x}) \cdot \hat{\mathbf{n}}]^2 - [(\mathbf{y} - \mathbf{x}) \cdot \hat{\mathbf{p}}]^2 \right) [T_n(\bar{\mathbf{x}})\hat{\mathbf{n}}] \right) d\mathbf{y}.
\end{aligned}$$

With a similar technique as in [Theorem 3.4](#) and with the $\delta/h = M$ assumption in M-convergence tests, we can show that each term in H_1 and H_2 is bounded by $O(1)$. \square

Remark 6. From the proof of [Theorem 4.2](#), we can see that in M-convergence tests either an $O(h)$ error on the provided traction load or an $O(h)$ error on the approximated unit normal and tangential vectors will induce an $O(1)$ truncation estimate in [\(3.3\)](#) for $\mathbf{x} \in \mathcal{I}\Omega_N$, which is of the same order generated by the proposed traction-type boundary condition formulation as discussed in [Theorem 3.4](#). Therefore, when using meshfree formulations and the broken bond techniques to induce damage as in [\[57\]](#), the proposed nonlocal traction loading formulation is of optimal asymptotic M-convergence rate to its local limit.

To sum up, with the meshfree discretization described above and the optimization-based quadrature weights $\omega_{j,i}$, $i = 1, \dots, N_p$, we solve for the displacement $\mathbf{u}(\mathbf{x}_i)$ and nonlocal dilatation θ_i from:

$$\mathbb{K}\eta = \mathbf{F}. \quad (4.11)$$

Here η is the vector of unknowns organized as follows:

$$\eta = [u_1, \dots, u_{DOF}, v_1, \dots, v_{DOF}, \theta_1, \dots, \theta_{DOF}]^T.$$

$DOF = \#\mathbf{x}_i : \mathbf{x}_i \in \Omega$ is the total number of material points to be solved, and u, v are the components of displacement such that $\mathbf{u}_i = [u_i, v_i]$. \mathbb{K} is a $3DOF \times 3DOF$ stiffness matrix. The right hand side \mathbf{F} is organized following a similar way as for η .

5. Numerical verification and asymptotic compatibility

In this section we numerically verify the approach by investigating accuracy when recovering analytic solutions in the M-convergence limit with mixed boundary conditions. We consider: linear patch tests, smooth manufactured solutions, analytical solutions to curvilinear surface loading problems, and analytical solutions to linearly elastic composites. For each case, we consider various combinations of Dirichlet and traction-type boundary conditions, exploring also the effect of reduced regularity on the traction problem by considering both Lipschitz and smooth boundaries. For each case we consider refinements of both Cartesian grids with mesh spacing h , and nonuniform grids generated by perturbing the Cartesian grids with a uniformly distributed random vector field $(\Delta x, \Delta y)$, $\Delta x, \Delta y \sim \mathcal{U}[-0.2h, 0.2h]$. For the sake of brevity we report the formal convergence study in the [Appendix](#), but summarize the setup and main conclusions for each case below, particularly focusing on whether optimal first order convergence in δ is realized as $\delta \rightarrow 0$, or if a lack of boundary regularity leads to suboptimal convergence. In all cases considered, the scheme does provide AC convergence as $\delta, h \rightarrow 0$.

5.1. Linear patch test

We consider as linear patch test the displacement

$$\mathbf{u}(x, y) = (3x + 2y, -x + 2y)$$

on a square domain $\Omega = [-\pi/2, \pi/2] \times [-\pi/2, \pi/2]$, with three different boundary conditions:

1. Full Dirichlet-type boundary conditions: $\partial\Omega_D = \partial\Omega$;
2. Mixed boundary conditions with traction loads applied on a straight line: $\partial\Omega_N = \{(x, \pi/2) | x \in [-\pi/2, \pi/2]\}$ and $\partial\Omega_D = \partial\Omega \setminus \partial\Omega_N$;
3. Mixed boundary conditions with traction loads applied on corner: $\partial\Omega_N = \{(x, \pi/2) | x \in [-\pi/2, \pi/2]\} \cup \{(\pi/2, y) | y \in [-\pi/2, \pi/2]\}$ and $\partial\Omega_D = \partial\Omega \setminus \partial\Omega_N$.

Note that in linear patch tests, the local and nonlocal solutions coincide. On settings 2 and 3, a traction-type boundary condition

$$\mathbf{T} = \begin{bmatrix} 5\lambda + 6\mu & \mu \\ \mu & 5\lambda + 4\mu \end{bmatrix} \mathbf{n} \quad (5.1)$$

is applied on the interface $\partial\Omega_N$, with material parameters following the plane strain assumption:

$$\lambda = K\nu/((1+\nu)(1-2\nu)), \mu = K/(2(1+\nu)),$$

for Young's modulus $K = 1$. Two values of Poisson ratio $\nu = 0.3$ and 0.49 are investigated which correspond to compressible and nearly-incompressible materials, respectively. To demonstrate independence of M -convergence rate to choice of M , we consider both $\delta = 3.5h$ and $\delta = 3.9h$. Note that in problems with the boundary condition setting 3, when \mathbf{x} is close to the corner the projection point $\bar{\mathbf{x}}$ is possibly ill-defined and therefore induces ambiguity of definition on $\mathbf{T}(\bar{\mathbf{x}})$. To resolve this possible issue, in setting 3 we define $\mathbf{T}(\bar{\mathbf{x}})$ following (5.1) where \mathbf{n} is the numerical approximation of normal direction following (4.9).

Uniform discretization: With settings 1 and 2, we observe that the numerical solution passes the patch test to within machine precision. Note that in setting 2, $\partial\Omega_N$ consists of a straight line and therefore $B_\delta(\mathbf{x}) \setminus \Omega$ is symmetric with respect to \mathbf{n} , and the numerical result is consistent with Theorem 3.3. In setting 3, $B_\delta(\mathbf{x}) \setminus \Omega$ is not symmetric when \mathbf{x} is close to the corner, and the numerical solution only passes the linear patch test approximately. In Fig. A.16, we compare $L^2(\Omega)$ error vs. h for displacement and dilatation to demonstrate first order AC convergence for both \mathbf{u} and θ , independent of δ/h and ν .

Non-uniform discretization: For a randomly perturbed grid, machine precision accuracy is again observed for setting 1 imposing full Dirichlet-type boundary conditions. With setting 2, the patch test is no longer satisfied as $B_\delta(\mathbf{x}) \setminus \Omega$ is generally asymmetric with respect to the background grid. We plot the $L^2(\Omega)$ errors of \mathbf{u} and θ vs. h in Fig. A.17. To investigate the impact of error in calculation of boundary normals, we present $L^2(\Omega)$ errors either approximately using the estimate from (4.9), or using the exact normals. From Fig. A.17, we observe an $O(h)$ convergence for the $L^2(\Omega)$ error of \mathbf{u} , and a deteriorated convergence rate for θ . When comparing the numerical results from approximated \mathbf{n} and exact \mathbf{n} , we surprisingly observed smaller numerical errors from the cases with approximate normal direction \mathbf{n} .

In Fig. A.18 we consider boundary condition setting 3. Since there is no analytical normal direction defined on the corner point, we only investigate the results from approximated normal unit vector through formulation (4.9). Comparing with the $O(h)$ convergence rate in the uniform discretization cases, setting 3 converges with suboptimal 0.75th order convergence for \mathbf{u} and 0.5th order for θ on non-uniform grids.

5.2. Manufactured solution test

To study the rate of convergence to the AC limit, we manufacture the local solution

$$\mathbf{u}_0(x, y) = [\sin(Ax) \sin(Ay), -\cos(Ax) \cos(Ay)]$$

by imposing forcing consistent with the local operator

$$\mathbf{f}(x, y) = [2(\lambda + 2\mu)A^2 \sin(Ax) \sin(Ay), -2(\lambda + 2\mu)A^2 \cos(Ax) \cos(Ay)].$$

A square domain $\Omega = [-\pi/2, \pi/2] \times [-\pi/2, \pi/2]$ and the three boundary condition settings described in the previous Section 5.1 are applied, to again consider the effect of boundary regularity. On $\mathcal{BB}\Omega_D$, the Dirichlet boundary condition $\mathbf{u}_D(x, y) = \mathbf{u}_0(x, y)$ is applied, while on the Neumann boundary we apply the traction condition

$$\mathbf{T}(x, y) = \begin{bmatrix} 2A(\lambda + \mu) \cos(A\pi/2) \sin(Ay) & 2A\mu \sin(A\pi/2) \cos(Ay) \\ 2A\mu \sin(Ax) \cos(A\pi/2) & 2A(\lambda + \mu) \cos(Ax) \sin(A\pi/2) \end{bmatrix} \mathbf{n}.$$

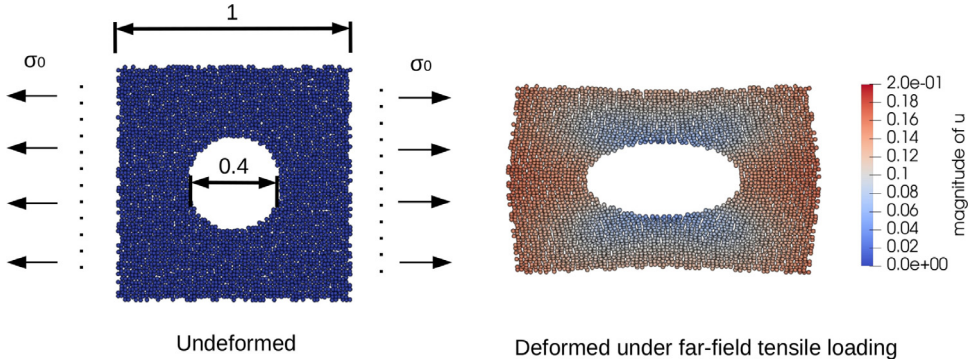


Fig. 4. Left: Problem settings for circular hole in an infinite solid under remote loading with spheres representing a non-uniformed discretization. Right: Final deformed object when taking the far-field tensile stress $\sigma_0 = 0.3$. (For interpretation of the references to color in this figure legend, the reader is referred to the web version of this article.)

We adopt material parameters under plane strain assumptions:

$$K = 1, \lambda = K\nu/((1+\nu)(1-2\nu)), \mu = K/(2(1+\nu)),$$

and compare Poisson ratios $\nu = 0.3$ or 0.49 again corresponding to compressible/near-incompressible limits. The parameter A is taken as 0.4 . For the possible ambiguity of projection point in setting 3, we set \mathbf{T} following a similar convention as in the linear patch test: for $\mathbf{x} \in \mathcal{I}\Omega_N$ close to the corner point $(\pi/2, \pi/2)$, we set $\mathbf{T}(\bar{\mathbf{x}}) \approx \mathbf{T}(\mathbf{x})$ where \mathbf{n} is numerically approximated with (4.9).

Uniform discretization: For Dirichlet boundary condition second-order convergence is achieved, consistent with the analysis in [Theorem 4.1](#) and the $L^2(\Omega)$ convergence results are presented in [Fig. A.19](#). For traction loadings on straight and corner boundaries (Settings 2 and 3), we present $L^2(\Omega)$ convergence results in [Fig. A.20](#) and [Fig. A.21](#), respectively. In these settings first-order convergence is observed for both \mathbf{u} and θ .

Non-uniform discretization: With non-uniform particle distribution, [Fig. A.22](#) demonstrates second-order $L^2(\Omega)$ convergence for both \mathbf{u} and θ under Setting 1. Under Setting 2, [Fig. A.23](#) demonstrates again first-order convergence. Again, somewhat surprisingly, when using the estimated normals one obtains improved accuracy, albeit with the same convergence rates. In [Fig. A.24](#), we further consider Setting 3 where $\partial\Omega_N$ includes a corner. Comparing with the results from uniform discretizations as shown in [Fig. A.21](#), a similar convergence rate ($O(h)$) is obtained for both \mathbf{u} and θ on non-uniform discretizations with setting 3.

5.3. Traction loading on curvilinear surfaces

We next consider more physical settings corresponding to homogeneous and inhomogeneous traction loadings on a curvilinear surface. Two different problems are considered:

1. We consider a free-surface circular hole of radius a in an infinite solid under remote loading σ_0 , as illustrated in [Fig. 4](#). Under a plane strain assumption the classical linear elasticity model yields the displacement field

$$\mathbf{u}_0(r, \theta) = \begin{pmatrix} \frac{\sigma_0 a}{8\mu} \left[\frac{r}{a}(\kappa + 1) \cos \theta + \frac{2a}{r} ((1 + \kappa) \cos \theta + \cos 3\theta) - \frac{2a^3}{r^3} \cos 3\theta \right] \\ \frac{\sigma_0 a}{8\mu} \left[\frac{r}{a}(\kappa - 3) \sin \theta + \frac{2a}{r} ((1 - \kappa) \sin \theta + \sin 3\theta) - \frac{2a^3}{r^3} \sin 3\theta \right] \end{pmatrix}. \quad (5.2)$$

where $\kappa = 3 - 4\nu$ and (r, θ) are the radial distance and azimuthal angle in cylindrical coordinates. To set the problem up, we impose the analytic local solution \mathbf{u}_0 as a Dirichlet-type condition on the nonlocal collar around the perimeter of a unit square. We then break all bonds crossing the circle of radius $a = 0.2$, and apply $\mathbf{T} = 0$ on the sharp interface $\partial\Omega_N = \{(x, y) | x^2 + y^2 = a^2\}$, fixing $\sigma_0 = 1$.

2. As an example of imposing non-zero traction loads, we consider the deformation of a hollow cylinder under an internal pressure p_0 , as illustrated in [Fig. 5](#). Under a plane strain assumption the classical linear elasticity

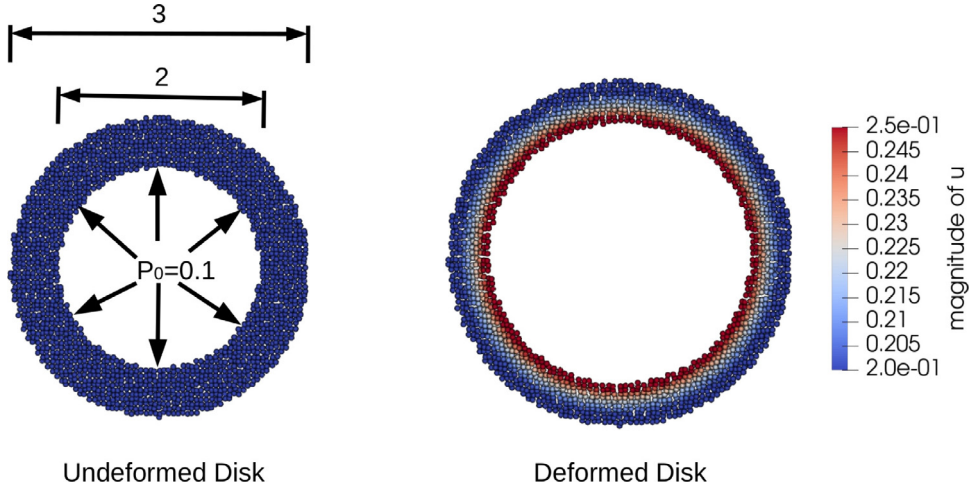


Fig. 5. Left: Problem settings for a hollow disk under internal pressure with spheres representing a non-uniform discretization. Right: Final deformed disk when taking the internal pressure $p_0 = 0.1$. (For interpretation of the references to color in this figure legend, the reader is referred to the web version of this article.)

model predicts displacements given by

$$\mathbf{u}_0(x, y) = \left[Ax + \frac{Bx}{x^2 + y^2}, Ay + \frac{By}{x^2 + y^2} \right]$$

where

$$A = \frac{(1 + \nu)(1 - 2\nu)p_0 R_0^2}{K(R_1^2 - R_0^2)}, \quad B = \frac{(1 + \nu)p_0 R_0^2 R_1^2}{K(R_1^2 - R_0^2)},$$

R_0 and R_1 are the interior and exterior radius of the hollow disk. Here we take $R_0 = 1$ and $R_1 = 1.5$. We impose the analytic local solution \mathbf{u}_0 as a Dirichlet-type condition on the nonlocal collar around the exterior boundary $\partial\Omega_D = \{(x, y) | x^2 + y^2 = R_1^2\}$ and break all bonds crossing the inner circle of radius $R_0 = 1$, and apply $\mathbf{T} = p_0 \mathbf{n}$ on the interface $\partial\Omega_N = \{(x, y) | x^2 + y^2 = R_0^2\}$. In all M-convergence tests we take $p_0 = 0.1$.

In the following tests we take the Young's modulus $K = 1$ and test with different Poisson ratios $\nu = 0.3$ and 0.49 . To investigate the asymptotic compatibility when $\delta/h = C$, we employ uniform and non-uniform discretizations and refine δ and h simultaneously while keeping the ratio δ/h a constant. In uniform discretizations, we take collocation points $X_h = \{(ah, bh), a, b \in \mathbb{N}\}$, and in non-uniform discretizations the uniform grid points are perturbed with $(\Delta x, \Delta y)$, $\Delta x, \Delta y \sim \mathcal{U}[-0.2h, 0.2h]$. Note here even with uniform discretizations, the collocation points do not align with $\partial\Omega_N$ since the latter is a circular curve, which introduces numerical errors as discussed in [Theorem 4.2](#). In both settings we also investigate performances of the proposed formulation with the approximated normal unit vector formulation [\(4.9\)](#) and the analytical normal direction.

Setting 1, Free circular surface: In [Fig. A.25](#) and [Fig. A.26](#), we demonstrate AC convergence for uniform and non-uniform particle distributions, respectively, for both compressible ($\nu = 0.3$) and incompressible ($\nu = 0.49$) materials. From the results, we observe first order convergence in the $L^2(\Omega)$ norm for the displacements in all cases. A deteriorated order of convergence is observed for θ , where a roughly 0.7th order is achieved for both uniform and non-uniform discretizations. When comparing the results with approximated \mathbf{n} and the results with analytical \mathbf{n} , the formulation with analytical \mathbf{n} performs similar or sometime slightly better than the results with approximated \mathbf{n} . Therefore, the formulation [\(4.9\)](#) still provides a reasonable numerical approximation for the normal unit vector \mathbf{n} .

Setting 2, Hollow disk under pressure: In [Figs. A.27](#) and [A.28](#), we present AC convergence for uniform and non-uniform particle configurations. We observe nearly first-order $L^2(\Omega)$ -norm convergence for displacements in both compressible and nearly-incompressible materials. Surprisingly, for nearly-incompressible materials, $O(h)$ order convergence is achieved for θ , but for compressible material a reduced order (around 0.65) convergence is

observed. Again, the convergence rates are nearly identical for analytical \mathbf{n} and approximated \mathbf{n} . Therefore, the approximation formulation (4.9) again provides a good practical estimate of \mathbf{n} .

5.4. Composite materials with discontinuous material properties

We now further consider an extension of the state-based peridynamics formulation (2.1) to composite materials constituted of n phases, so that the domain may be partitioned into disjoint subdomains with piecewise constant material properties, i.e. $\Omega = \cup_k \Omega_k$, $\Omega_k \cap \Omega_l = \emptyset$, and $\lambda(\mathbf{x}) = \lambda_k$, $\mu(\mathbf{x}) = \mu_k$ for $\mathbf{x} \in \Omega_k$. Discussions on the mathematical properties of this heterogeneous system can be found in, e.g., [58]. Specifically, when $\lambda(\mathbf{x})$ and $\mu(\mathbf{x})$ may vary for each material point \mathbf{x} , we propose the following formulation:

$$\begin{aligned} \mathcal{L}_\delta \mathbf{u} := & -\frac{C_\alpha}{m(\delta)} \int_{B_\delta(\mathbf{x})} (\lambda(\mathbf{x}, \mathbf{y}) - \mu(\mathbf{x}, \mathbf{y})) K(|\mathbf{y} - \mathbf{x}|) (\mathbf{y} - \mathbf{x}) (\theta(\mathbf{x}) + \theta(\mathbf{y})) d\mathbf{y} \\ & - \frac{C_\beta}{m(\delta)} \int_{B_\delta(\mathbf{x})} \mu(\mathbf{x}, \mathbf{y}) K(|\mathbf{y} - \mathbf{x}|) \frac{(\mathbf{y} - \mathbf{x}) \otimes (\mathbf{y} - \mathbf{x})}{|\mathbf{y} - \mathbf{x}|^2} (\mathbf{u}(\mathbf{y}) - \mathbf{u}(\mathbf{x})) d\mathbf{y} = \mathbf{f}(\mathbf{x}), \end{aligned} \quad (5.3)$$

where the two-point functions $\mu(\cdot, \cdot)$, $\lambda(\cdot, \cdot)$ denote averaged material properties satisfying $\mu(\mathbf{z}, \mathbf{z}) = \mu(\mathbf{z})$ and $\lambda(\mathbf{z}, \mathbf{z}) = \lambda(\mathbf{z})$. We will consider for the purposes of this work the harmonic mean

$$\frac{2}{\mu(\mathbf{x}, \mathbf{y})} = \frac{1}{\mu(\mathbf{x})} + \frac{1}{\mu(\mathbf{y})}, \quad \frac{2}{\lambda(\mathbf{x}, \mathbf{y})} = \frac{1}{\lambda(\mathbf{x})} + \frac{1}{\lambda(\mathbf{y})}. \quad (5.4)$$

Correspondingly, to evaluate the above formulation, we modify the meshfree formulation with optimization-based quadrature weights in (4.1) as follows:

$$\begin{aligned} & -\frac{C_\alpha}{m(\delta)} \sum_{\mathbf{x}_j \in B_\delta(\mathbf{x}_i)} (\lambda_{ij} - \mu_{ij}) K_{ij} (\mathbf{x}_j - \mathbf{x}_i) (\theta_i + \theta_j) \omega_{j,i} \\ & - \frac{C_\beta}{m(\delta)} \sum_{\mathbf{x}_j \in B_\delta(\mathbf{x}_i)} \mu_{ij} K_{ij} \frac{(\mathbf{x}_j - \mathbf{x}_i) \otimes (\mathbf{x}_j - \mathbf{x}_i)}{|\mathbf{x}_j - \mathbf{x}_i|^2} \cdot (\mathbf{u}_j - \mathbf{u}_i) \omega_{j,i} = \mathbf{f}_i, \end{aligned} \quad (5.5)$$

where $\lambda_{ij} := \lambda(\mathbf{x}_i, \mathbf{x}_j)$ and $\mu_{ij} := \mu(\mathbf{x}_i, \mathbf{x}_j)$.

We numerically investigate the AC convergence of the nonlocal solution for a hydrostatically loaded cylindrical inclusion of radius a in an infinite plate. We denote the interior of the inclusion as Ω_1 and the exterior as Ω_2 , with corresponding constant material properties (μ_1, λ_1) and (μ_2, λ_2) . Assuming a far-field hydrostatic stress P_∞ and plane strain conditions, we define the coefficients

$$\begin{aligned} C_A &= \frac{P_\infty}{2(\lambda_1 + \mu_1)}, \\ C_B &= \frac{P_\infty (\lambda_1 + \mu_1 + \mu_2)}{2(\lambda_1 + \mu_1)(\lambda_2 + 2\mu_2)}, \\ C_C &= -\frac{P_\infty d^2 (\lambda_1 - \lambda_2 + \mu_1 - \mu_2)}{2(\lambda_1 + \mu_1)(\lambda_2 + 2\mu_2)}, \end{aligned}$$

and the analytic local solution for the displacement field in cylindrical coordinates is given by

$$u_r = \begin{cases} C_A r & \mathbf{x} \in \Omega_1, \\ C_B r + C_C/r & \mathbf{x} \in \Omega_2, \end{cases} \quad u_\theta = 0.$$

We use this solution to assess the stability of the method in the vicinity of large jumps in material properties — for such scenarios high-order meshfree reconstructions have been shown to demonstrate unphysical oscillations near material interfaces [59]. Note that the consistency conditions derived only guarantee asymptotic compatibility under the assumption of an isotropic material; this benchmark thus explores the applicability of the approach beyond the guarantees of the approximation theory in Theorem 4.1.

We first investigate whether the discretization is AC. We take $a = 0.2$, impose a jump in the bulk modulus ($K_1 = 2$, $K_2 = 1$), and apply the analytic local solution \mathbf{u}_0 as a Dirichlet-type condition on the nonlocal collar around the perimeter of a unit square. We consider three scenarios corresponding to different material compressibilities: (1)

$\nu_1 = \nu_2 = 0.25$, (2) $\nu_1 = \nu_2 = 0.49$ and (3) $\nu_1 = 0.49$, $\nu_2 = 0.25$. We present $L^2(\Omega)$ convergence for both uniform and randomly perturbed particle distributions in Fig. A.29 and Fig. A.30 respectively. For both scenarios, for all three Poisson ratio combinations we obtain first- and half-order convergence for the displacement and dilatation, respectively.

We next investigate the stability of the approach over a large range of material parameters. To do this, we set $\mu_1 = 1$ and fix the Poisson ratio in both phases to $\nu_1 = \nu_2 = \frac{1}{4}$ and impose a jump in the Young's modulus of $K_2/K_1 = Q$, for $Q \in \{2^{-8}, 2^8\}$. In these tests we employ a square domain $\Omega := [-\pi/2, \pi/2] \times [-\pi/2, \pi/2]$ and apply the analytic local solution \mathbf{u}_0 as a Dirichlet-type condition on the nonlocal collar around the perimeter of Ω . In Fig. 6, we plot a profile of the x-component of displacement along the $y = 0$ line to provide a qualitative assessment of the solution. We demonstrate convergence for both a stiff inclusion ($K_1 = 64K_2$), a soft inclusion ($K_2 = 64K_1$), and then illustrate that we reproduce well the displacement for a wide range of parameters.

6. Fracture dynamics for brittle fracture experiments

The previous sections have established the ability of the scheme to recover local solutions of boundary value problems in elasticity governed by traction loadings and ensured that the breaking bonds treatment does not impair the AC convergence of the quadrature treatment. Of course, the main appeal of peridynamic discretizations is to handle fracture problems, and we devote the remainder of the paper to demonstrating how the scheme prescribed previously adapts to practical engineering settings, where now free surfaces are associated with the time evolution of a fracture surface. We specifically consider brittle fracture mechanics in linearly elastic materials and provide validation against experiment and existing numerical results. The main objective of this section is to provide a proof-of-principle demonstration that the framework introduced thus far applies to realistic settings, however overall the provided preliminary validation provides good agreement.

In this section we introduce an inertial term to handle dynamics

$$\left\{ \begin{array}{ll} \rho \frac{\partial^2 \mathbf{u}(\mathbf{x}, t)}{\partial t^2} + \mathcal{L}_\delta \mathbf{u}(\mathbf{x}, t) = \mathbf{f}(\mathbf{x}, t), & \text{for } (\mathbf{x}, t) \in \Omega \setminus \mathcal{I}\Omega_N \times [0, T], \\ \rho \frac{\partial^2 \mathbf{u}(\mathbf{x}, t)}{\partial t^2} + \mathcal{L}_{N\delta} \mathbf{u}(\mathbf{x}, t) = \mathbf{f}_{N\delta}(\mathbf{x}, t), & \text{for } (\mathbf{x}, t) \in \mathcal{I}\Omega_N \times [0, T], \\ \theta(\mathbf{x}, t) = \frac{d}{m(\delta)} \int_{B_\delta(\mathbf{x})} K(|\mathbf{y} - \mathbf{x}|) (\mathbf{y} - \mathbf{x})^T (\mathbf{u}(\mathbf{y}, t) - \mathbf{u}(\mathbf{x}, t)) d\mathbf{y}, & \text{for } (\mathbf{x}, t) \in (\Omega \cup \mathcal{B}\Omega_D \setminus \mathcal{I}\Omega_N) \times [0, T], \\ \theta(\mathbf{x}, t) = \frac{d}{m(\delta)} \int_{B_\delta(\mathbf{x}) \cap \Omega} K(|\mathbf{y} - \mathbf{x}|) (\mathbf{y} - \mathbf{x})^T \mathbf{M}(\mathbf{x}) (\mathbf{u}(\mathbf{y}, t) - \mathbf{u}(\mathbf{x}, t)) d\mathbf{y}, & \text{for } (\mathbf{x}, t) \in \mathcal{I}\Omega_N \times [0, T], \\ \mathbf{u}(\mathbf{x}, t) = \mathbf{u}_D(\mathbf{x}, t), & \text{for } (\mathbf{x}, t) \in \mathcal{B}\mathcal{B}\Omega_D \times [0, T], \\ \mathbf{u}(\mathbf{x}, 0) = \mathbf{u}_{IC}(\mathbf{x}), \quad \frac{\partial \mathbf{u}(\mathbf{x}, 0)}{\partial t} = \mathbf{v}_{IC}(\mathbf{x}), \quad \frac{\partial^2 \mathbf{u}(\mathbf{x}, 0)}{\partial t^2} = \mathbf{w}_{IC}(\mathbf{x}), & \text{for } \mathbf{x} \in \Omega \cup \mathcal{B}\mathcal{B}\Omega_D, \end{array} \right. \quad (6.1)$$

where ρ is the material density and \mathbf{u}_{IC} , \mathbf{v}_{IC} , \mathbf{w}_{IC} are the initial displacement, velocity and acceleration fields, respectively. To model brittle fracture, for $\mathbf{x}_j \in B_\delta(\mathbf{x}_i)$ we break the bond between \mathbf{x}_i and \mathbf{x}_j when the associated strain exceeds a critical strain criteria s_0 :

$$s_{ij} := \frac{\|\mathbf{u}_j - \mathbf{u}_i + \mathbf{x}_j - \mathbf{x}_i\| - \|\mathbf{x}_j - \mathbf{x}_i\|}{\|\mathbf{x}_j - \mathbf{x}_i\|} > s_0. \quad (6.2)$$

We employ the criteria derived in [60] relating s_0 to material parameters:

$$s_0 = \sqrt{\frac{G_0}{4(\lambda - \mu)\beta' + 8\mu\beta}}, \quad (6.3)$$

where $\beta = \frac{3\delta}{4\pi}$, $\beta' = 0.23873\delta$, and G_0 is the critical energy release rate or fracture energy. For $\mathbf{x}_j \in B_\delta(\mathbf{x}_i)$, this damage criterion can be implemented by replacing the static state weight $\gamma_{j,i}$ in (4.5) with a history-dependent scalar boolean state function $\gamma_{j,i}(t)$:

$$\gamma_{j,i}(t) = \begin{cases} 1, & \text{if } s_{ij}(\tau) \leq s_0, \quad \forall \tau \leq t, \text{ and } \mathbf{x}_j \in B_\delta(\mathbf{x}_i) \cap \Omega, \\ 0, & \text{otherwise,} \end{cases}$$

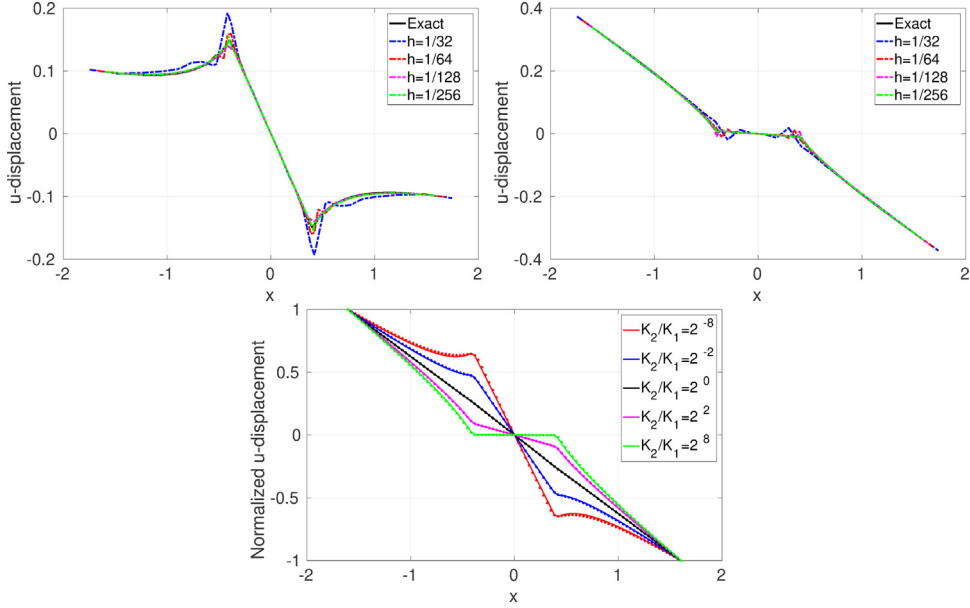


Fig. 6. Displacements across the $y = 0$ line, comparing prediction to analytic solution for composite problem. Upper left: Convergence to analytic solution for a soft inclusion ($K_2/K_1 = 1/64$). Upper right: Convergence to analytic solution for a stiff inclusion ($K_2/K_1 = 64$). Bottom: For a fixed resolution of 64^2 points, reproduction of analytic solution for a wide range of $K_2/K_1 \in (2^{-8}, 2^8)$. Solid line corresponds to analytic solution, while dots correspond to numerical result. (For interpretation of the references to color in this figure legend, the reader is referred to the web version of this article.)

such that $\tilde{\omega}_{j,i} = \omega_{j,i}\gamma_{j,i}(t)$, $\hat{\omega}_{j,i} = \omega_{j,i}(1 - \gamma_{j,i}(t))$. To postprocess fracture evolution and identify cracks, we define the damage as

$$\phi_i(t) = \frac{\sum_{\mathbf{x}_j \in B(\mathbf{x}_i)} (1 - \gamma_{j,i}(t))}{\sum_{\mathbf{x}_j \in B(\mathbf{x}_i)} 1}. \quad (6.4)$$

For the purposes of fracture identification, we say that a crack occurs at \mathbf{x}_i if ϕ_i exceeds 0.35. This threshold is somewhat arbitrary, but necessary to, e.g., postprocess the crack propagation velocity at which a crack grows.

To discretize we apply the Newmark scheme together with the meshfree quadrature established previously

$$\left\{ \begin{array}{ll} \frac{4\rho}{\Delta t^2} \ddot{\mathbf{u}}_i^{n+1} + (\mathcal{L}_\delta^h \mathbf{U})_i^{n+1} = \mathbf{f}_i^{n+1} + \frac{4\rho}{\Delta t^2} (\mathbf{u}_i^n + \Delta t \dot{\mathbf{u}}_i^n + \frac{\Delta t^2}{4} \ddot{\mathbf{u}}_i^n), & \text{for } \mathbf{x}_i \text{ in } \Omega \setminus \mathcal{I}\Omega_N^{n+1}, \\ \frac{4\rho}{\Delta t^2} \ddot{\mathbf{u}}_i^{n+1} + (\mathcal{L}_{N\delta}^h \mathbf{u})_i^{n+1} = (\mathbf{f}_{N\delta}^h)_i^{n+1} + \frac{4\rho}{\Delta t^2} (\mathbf{u}_i^n + \Delta t \dot{\mathbf{u}}_i^n + \frac{\Delta t^2}{4} \ddot{\mathbf{u}}_i^n), & \text{for } \mathbf{x}_i \text{ in } \mathcal{I}\Omega_N^{n+1}, \\ \theta_i^{n+1} = \frac{d}{m(\delta)} \sum_{\mathbf{x}_j \in B_\delta(\mathbf{x}_i)} K_{ij}(\mathbf{x}_j - \mathbf{x}_i)^T (\mathbf{u}_j^{n+1} - \mathbf{u}_i^{n+1}) \omega_{j,i}, & \text{for } \mathbf{x}_i \text{ in } \Omega \cup \mathcal{B}\Omega_D \setminus \mathcal{I}\Omega_N^{n+1}, \\ \theta_i^{n+1} = \frac{d}{m(\delta)} \sum_{\mathbf{x}_j \in B_\delta(\mathbf{x}_i)} K_{ij}(\mathbf{x}_j - \mathbf{x}_i)^T \mathbf{M}_i (\mathbf{u}_j^{n+1} - \mathbf{u}_i^{n+1}) \tilde{\omega}_{j,i}, & \text{for } \mathbf{x}_i \text{ in } \mathcal{I}\Omega_N^{n+1}, \\ \mathbf{u}_i^{n+1} = \mathbf{u}_D(\mathbf{x}_i), & \text{for } \mathbf{x}_i \text{ in } \mathcal{B}\mathcal{B}\Omega_D, \end{array} \right. \quad (6.5)$$

where Δt is the time step size, $\mathbf{f}_i^{n+1} := \mathbf{f}(\mathbf{x}_i, t^{n+1})$, \mathcal{L}_δ^h and $\mathcal{L}_{N\delta}^h$ are the discretized nonlocal operators as defined in (4.1) and (4.6), respectively, and $\mathbf{f}_{N\delta}^h$ is also as defined in (4.6). The acceleration and velocity at the $n+1$ th time step are then calculated as follows:

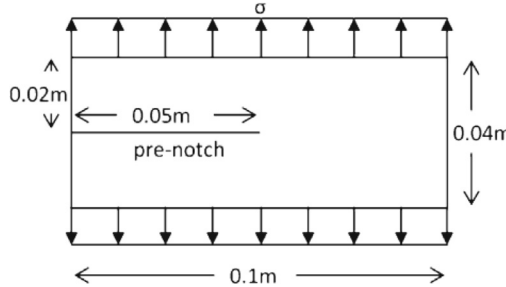
$$\ddot{\mathbf{u}}_i^{n+1} := \frac{4}{\Delta t^2} (\mathbf{u}_i^{n+1} - \mathbf{u}_i^n - \Delta t \dot{\mathbf{u}}_i^n) - \ddot{\mathbf{u}}_i^n, \quad \dot{\mathbf{u}}_i^{n+1} := \dot{\mathbf{u}}_i^n + \frac{\Delta t}{2} (\ddot{\mathbf{u}}_i^n + \ddot{\mathbf{u}}_i^{n+1}).$$

Note that because the evolving fracture creates new free surfaces, $\partial\Omega_N$ and $\mathcal{I}\Omega_N$ alter with time. To capture the implicit coupling between the material response and the evolving geometry due to fracture evolution, we employ

Table 1

Material properties used in pre-cracked soda-lime glass experiment.

Young's modulus E	Poisson ratio ν	Density ρ	Fracture energy G_0
72 GPa	0.23	2440 kg/m ³	3.8 J/m ²

**Fig. 7.** Problem setup for pre-cracked soda-lime glass experiment under tensile loading, following [63].

subiterations at each time step as follows. We first assume no new bonds have been broken at the current time step and solve for the displacement field. Based on the displacement field, we evaluate the damage criteria (6.2) for each bond. If any bond meets the criteria of breaking, we break all these bonds, update the corresponding state functions $\gamma_{j,i}$ and quadrature weights $\hat{\omega}_{j,i}$ and $\tilde{\omega}_{j,i}$, then solve for the displacement field again with new free surfaces. We repeat this procedure until no new broken bonds are detected, and finally proceed to the next time step.

We consider three benchmark problems involving material damage. In Sections 6.1–6.2 we study dynamic crack propagation and branching in glass. In Section 6.1, we adopt the benchmark problem from [61] and simulate a pre-cracked glass plate under sudden tensile loading. In Section 6.2, we reproduce a recent experiment considering V-notched glass samples impacted by a striker [62]. In Section 6.3, we simulate the material fragmentation of a cylinder under internal pressure and identify the number of fragments.

6.1. Dynamic brittle fracture I: Pre-cracked glass under tensile loading

We first investigate the crack propagation and branching of soda-lime glass as a prototypical brittle fracture exemplar, whereby a pre-notched thin rectangular plate is subject to tensile loads on its top and bottom (Fig. 7). Following the setup in [63], we consider plate dimensions of 0.1 m by 0.04 m with an initial crack of length 0.05 m, and a constant tensile load $\sigma = 2$ MPa applied on the top and bottom of the sample starting at $T = 0$. All other boundaries, including the new boundaries created by cracks, are treated as free surfaces. The mechanical properties of soda-lime glass are listed in Table 1. This problem was studied in several numerical studies on bond-based peridynamics [37,63,64] and non-ordinary state-based peridynamics [65] (see [26] for a review). Experimentally the crack propagation speed is fairly reproducible and was reported as 1580 m/s in [66]. To validate our scheme's ability to reproduce crack propagation speed and branching location we compare against available numerical and experimental results from [61,63,66].

We first plot in Fig. 8 the fracture evolution based on a uniform grid spacing with $h = 5 \times 10^{-4}$ m, $\delta = 4h$ and $\Delta t = 6.25 \times 10^{-2}$ μ s. A qualitative comparison to the results from [61, Figure 5] shows that we qualitatively recover the same dynamics as existing simulations, independent of particle distribution.

For engineering applications, non-uniform discretizations are desirable to handle complex geometries and establish grid independence. For many discretizations, so-called grid-imprinting may qualitatively numerically skew fracture patterns so that they correlate with mesh orientation and special care is often required in numerical methods [30,61]. To this end, we compare the effect of particle anisotropy on the resulting fracture, comparing our approach to a popular meshfree quadrature rule from designed for Cartesian particle distributions [25,68]. We also compare against a mesh-based approach, building a Delaunay mesh on a Cartesian grid with nodal spacing h and assigning particles at cell centroids with quadrature weight equal to the cell measure [64,67]. We generate non-uniform discretizations by perturbing either the particle locations or Delaunay nodes by $0.2h$, and consider

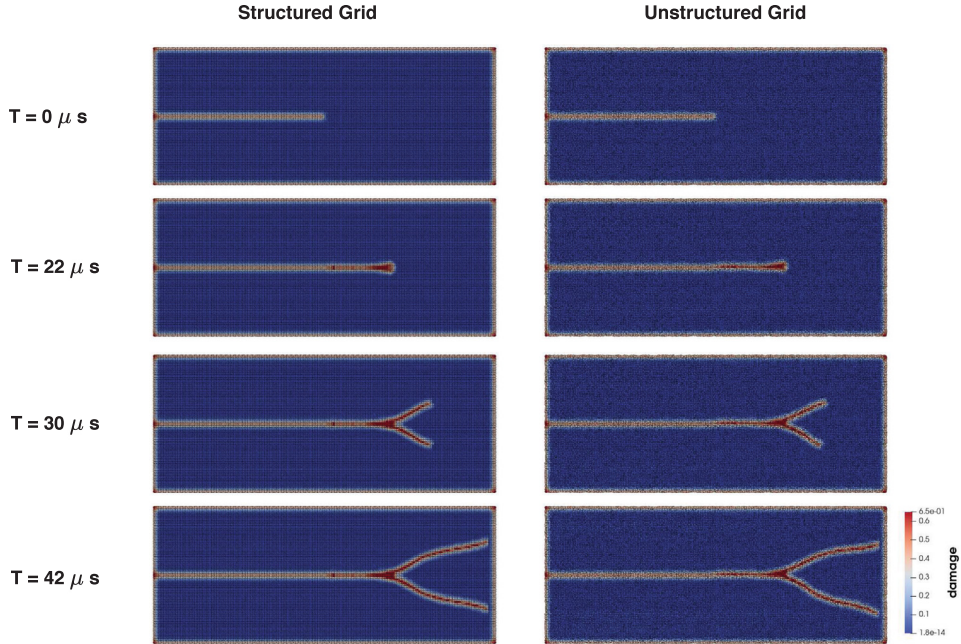


Fig. 8. Simulated damage evolution of pre-cracked soda-lime glass crack branching study, using resolution $h = 0.0005$ m and $\delta = 0.002$ m. *Left:* uniform discretization, *Right:* non-uniform discretization. (For interpretation of the references to color in this figure legend, the reader is referred to the web version of this article.)

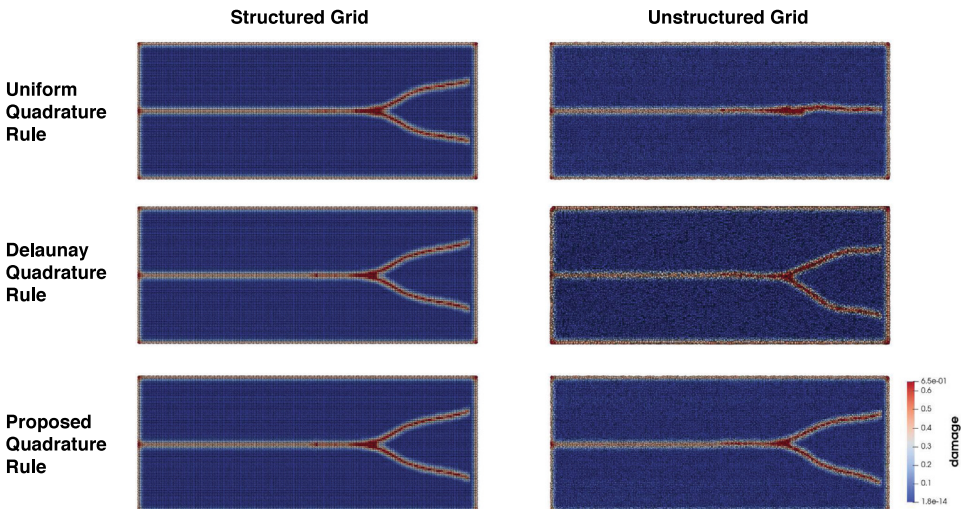


Fig. 9. Simulated fracture pattern at $T = 42$ μ s for pre-cracked soda-lime glass crack branching study, using various quadrature strategies and resolution $h = 0.0005$ m, $\delta = 0.002$ m. *Left:* uniform discretization, *Right:* non-uniform discretization. For non-uniform grids, the proposed meshfree approach predicts branching in line with a Delaunay mesh-based discretization [64,67]. (For interpretation of the references to color in this figure legend, the reader is referred to the web version of this article.)

$h = 5 \times 10^{-4}$ m. Ideally, we would hope to recover results comparable to the mesh-based approach on non-uniform discretizations, without the need to introduce a mesh into the problem. By comparing the corresponding fracture patterns in Figs. 8 and 9, we can see that with our proposed meshfree scheme is more robust to particle anisotropy than traditional meshfree quadrature, providing nearly identical results on uniform or nonuniform grids.

Table 2

Quantitative comparison of crack dynamics to existing experimental and numerical works. Here “Exp” stands for experimental results from [66], “BB” is the estimated result with the bond-based peridynamics measured from [63], and “SB” corresponds to the current approach with the state-based peridynamics.

Quantity	Exp	BB ($\delta = 2e-3m$)	BB ($\delta = 5e-4m$)	SB ($\delta = 2e-3m$)	SB ($\delta = 1e-3m$)
Branching Location (m)	–	0.065	0.068	0.070	0.068
Branching Time (μs)	–	23.0	21.5	21.8	22.5
Max Prop Speed (m/s)	1580	2000	1679	2250	2000

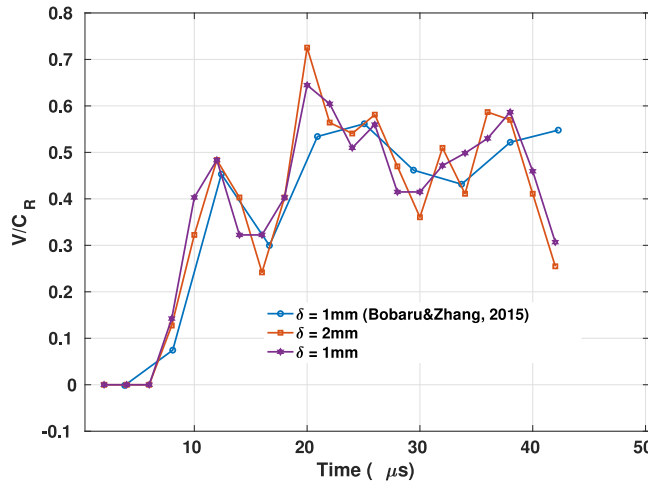


Fig. 10. Comparison of the soda-lime glass (normalized) crack propagation speed: proposed formulation versus numerical results reported in [61]. (For interpretation of the references to color in this figure legend, the reader is referred to the web version of this article.)

To quantitatively validate our simulation results, we validate the time and location of crack branching and the crack propagation speed and compare against [61,63,66]. In all experiments, we kept a fixed time step size $\Delta t = 6.25 \times 10^{-2} \mu s$ and a fixed ratio $\delta/h = 4$. Theoretically, the nonlocal length scale in state-based peridynamics should be smaller than geometrical features to prevent unrealistic nonlocal interactions. Therefore, we also investigate the M-convergence test by decreasing h and δ simultaneous to see if crack propagation features converge, considering $h = 5 \times 10^{-4} m$ and $h = 2.5 \times 10^{-4} m$. In Table 2, we compare these quantities of interest against numerical and experimental data. We obtain good agreement for the branching time and location, but overestimate the maximum speed. This may be a result of under-resolution, as the overestimation is reduced under refinement. However, we note that several other methods [26,64,65] achieve similar results. To conclusively establish an improvement in the current formulation regarding this quantity of interest, we defer a deeper investigation of this discrepancy to an upcoming work involving a parallel implementation of the current scheme allowing a more involved refinement study.

In Fig. 10 we plot the predicted crack propagation speeds under different δ as functions of time, and compare them with the numerical results from [63]. All results are normalized by the Rayleigh wave speed $c_R = 3102 m/s$. We can observe that the numerical simulation shows a similar trend: prior to the crack entering the branching phase, the speed gradually decreases, and then rapidly increases after branching. These trends are also observed in experiments [62,69].

6.2. Dynamic brittle fracture II: V-notched glass under impact

Recently, Dondeti and Tippur have studied impact-induced crack branching experiments on soda-lime glass by applying three prevalent optical techniques: transmission photoelasticity, 2D Digital Image Correlation (DIC) and transmission Digital Gradient Sensing (DGS) [62]. Following the setup sketched in Fig. 11, a Hopkinson pressure bar was used to impart a impulse upon a V-notch and study the resulting fracture — we defer to [62] for further

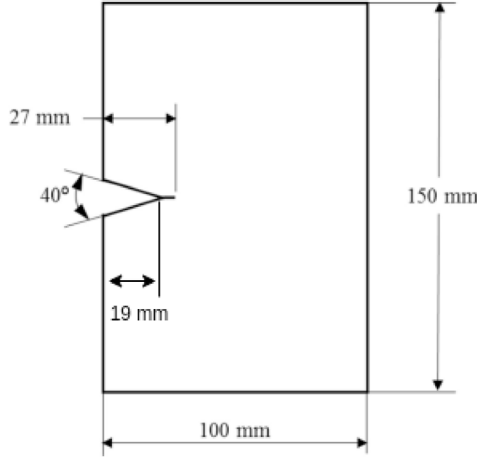


Fig. 11. Problem setup for V-notched soda-lime glass specimen under impact, following [62].

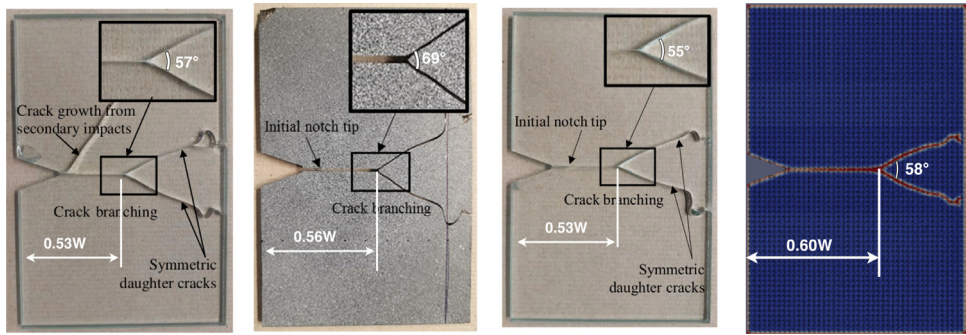


Fig. 12. Experimental fracture patterns and comparison to numerical prediction for V-notch case. From left to right: experimental results from photoelasticity in [62]; experimental results from Digital Image Correlation (DIC) in [62]; experimental results from Digital Gradient Sensing (DGS) in [62]; numerical simulation results from the proposed approach. (For interpretation of the references to color in this figure legend, the reader is referred to the web version of this article.)

Table 3

Mechanical properties for V-notched soda-lime glass specimens taken from [62].

Young's modulus E	Poisson ratio ν	Density ρ	Fracture energy G_0
70 GPa	0.22	2500 kg/m ³	8 J/m ²

details of the experimental setup. Three nominally identical but separate experiments were carried out to compare three different optical techniques in [62], and the experimental results are reproduced here in the first three plots of Fig. 12. Although the branching location and the branching angles were not reported in [62], we used the photographs shown in Fig. 12 to measure branch locations and angles to serve as validation data. For the three specimens, crack branching was observed at 53%, 56%, and 53% of the width, with branching angles as 57°, 69°, and 55°, respectively. Moreover, one can observe that in all specimens the crack path presents small oscillations near the far end of the sample due to wave reflections/spalling, which we aim to reproduce.

In this experiment, detailed information regarding contact force history, crack propagation speed, branching angle and point of branching are provided, allowing validation of numerical simulations against experiment using identical experimental loading conditions. In Table 3 we list the material properties of soda-lime glass as provided in [62], where the fracture energy $G_0 = 8 \text{ J/m}^2$ is measured during the experiment using the DGS technique when crack initiates. The force histories on the V-notch faces of the specimen by the long-bar were evaluated with DGS, as

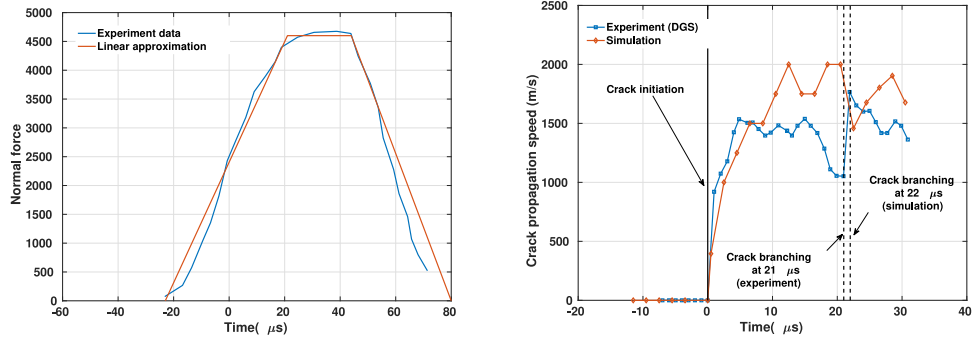


Fig. 13. Left: Normal force loads applied to V-notch, demonstrating forces measured from experiment (DGS) (reproduced from [62]) and approximate piecewise linear load applied in simulations. Right: Crack speed profiles, comparing experimental results (DGS) (reproduced from [62]) to numerical prediction. Time is denoted after the onset of branching. (For interpretation of the references to color in this figure legend, the reader is referred to the web version of this article.)

reproduced in blue in the left plot of Fig. 13. In our numerical simulations, a piecewise linear approximation of the applied normal force is applied uniformly over the V-notch surface as a time-varying traction load. Following the settings in [62], the frictional effect is neglected. Moreover, since the actual measurement of the bar tip shape was not provided in experiments, we assume that the full length of the V-notch is loaded, although we note that the predicted failure patterns might differ from the ones produced by the partial loading of the notch surfaces [70]. Crack velocities were also estimated in [62], and the results indicate that both the photoelastic recording and the DGS method provided reliable velocity history profiles.

To simulate the experiment, plane stress assumptions are adopted and traction loads are applied consistent with the experimentally measured normal force at the V-notch and free surfaces over the remainder of the boundary. A uniform discretization is employed with grid size $h = 0.5$ mm, and we select horizon $\delta = 4h$, and time step $\Delta t = 0.125$ μs. The predicted fracture pattern and crack velocity profile is given in Fig. 12 and Fig. 13, respectively. In Fig. 12, results show that branching happens at location 60% away from the left edge of the sample, with a branching angle of around 58°. While the branching angle matches very well within the range of angles from experimental measurements (55°–69°), the branching location is a little further than the measurements in experiment (53%–56%), in what follows we explore possible explanations. Oscillations in the fracture surface are reproduced near the back of the specimen. In Fig. 13 we provide comparisons of the crack speed as a function of time.

For the results provided, the results provide qualitative agreement sufficient for the purposes of this work. We do offer speculation regarding possible explanation and areas which may lead to improved quantitative agreement. Regarding the discrepancy in branching location, Mehrmashhadi et al. was able to achieve better agreement with experiment by applying the normal force loading over a subset of the full V-notch, to model the effect of reduced area under contact [70]. We remark that we were able to achieve improved agreement in crack branching location with similar techniques. We omit any results along these lines however, as our focus is only to demonstrate our boundary treatment for a realistic problem and a careful analysis of physical modeling assumptions is beyond the scope of this work. We also note that Mehrmashhadi et al. was able to employ a finer mesh; again we defer a careful analysis of such effects to a future work where we introduce a scalable implementation.

Next we characterize the reproducibility of the predicted crack paths, considering in particular the effect of anisotropy in the underlying discretization. For an increasing magnitude of perturbation ratio $r \in (0, 1)$, a quasi-uniform pointset is generated by perturbing every point in the uniform grid by a uniformly distributed random variable of magnitude rh . In this study we take $h = 0.5$ mm, $\Delta t = 0.125$ μs, $\delta = 2$ mm and $r \in \{0.01, 0.03, 0.05, 0.1, 0.15, 0.2\}$. For each r , we calculate solutions corresponding to 20 non-uniform particle distributions. To investigate the impact of non-uniform grids on crack features, we record the branching location and branching angle, and report their means and standard errors versus the grid perturbation ratio r in Fig. 14.

For the branching location, all simulations predict fairly consistent results: the crack starts to branch at around 60%–62% of the specimen width. Larger variations are observed on the branching angle when $r \geq 0.03$, which is

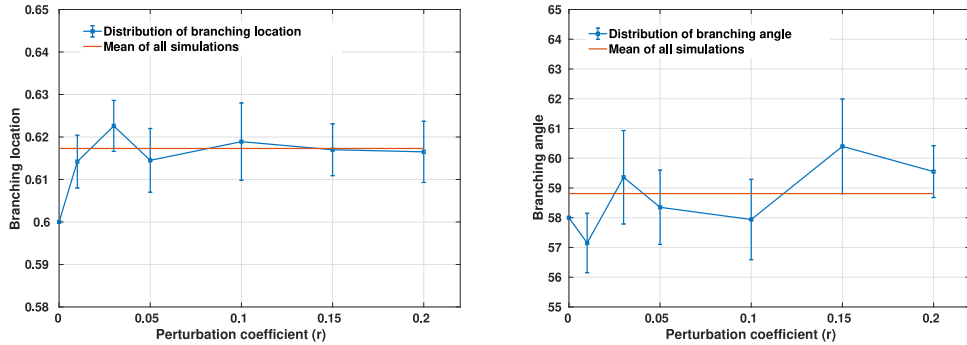


Fig. 14. Reproducibility and effect of anisotropy in spatial location of crack branching point. Non-uniform discretizations are employed by perturbing the uniform particle locations by rh , $r \in [0, 0.2]$. Left: Mean and standard error of predicted branching location. Right: Mean and standard error of branching angles.

Table 4

Mechanical properties for the cylinder fragmentation under internal pressure example, following [71,72].

Material properties	Young's modulus E	Poisson ratio ν	Density ρ	Fracture energy G_0
Value	200 GPa	0.3	7800 kg/m ³	1.125×10^5 J/m ²

Table 5

Predicted number of large and small fragments in the cylinder under internal pressure simulation.

Number of particles	Number of large fragments	Number of small fragments
3124	12	2
12 587	15	3
22 413	15	9
35 035	14	4

possibly due to the fact that these estimates are sensitive to the placement of the branching points. Across all r , a mean angle with 57° – 60° is predicted, which lies in the range observed from experiments (55° – 69°). The numerical results indicate that these crack features are not overly sensitive to small perturbations in the discretization grids, demonstrating the suitability of the scheme to handle nontrivial problems without imparting grid anisotropy effects on the resulting fracture prediction.

6.3. Fragmentation of cylinder expansion

In the last example simulation, we consider the fragmentation of a cylinder under internal pressure, so as to evaluate the proposed algorithm on handling multiple cracks and fragments. Following a similar setting as in [71], a cylinder with inner radius 80 mm and outer radius 150 mm is employed, with material properties listed in Table 4. The cylinder is subject to an internal $p = p_0 e^{-t/t_0}$, where $p_0 = 2.5$ GPa, and $t_0 = 0.01$ ms. We run the simulation with $\delta = 4h$, $\Delta t = 0.05$ μ s, and four different levels of spatial resolution: 3124, 12 587, 22 413, and 35 035 discretization points (particles). For each set of discretization points, we generate non-uniform grids by perturbing particle positions by a uniformly distributed perturbation of magnitude $0.2h$. In Fig. 15, we show simulation results at $T = 0.2$ ms, when the cylinder breaks into fragments. The number of large and small fragments are listed in Table 5, where we can observe that the number of large fragments is generally consistent except for the case with the coarsest resolution. The number of small fragments generally increases when using finer discretizations but it is not monotonic. These observations as well as the number of large fragments are consistent with the simulation results in [71], where a particle model was employed and 15–16 numbers of large fragments were predicted in

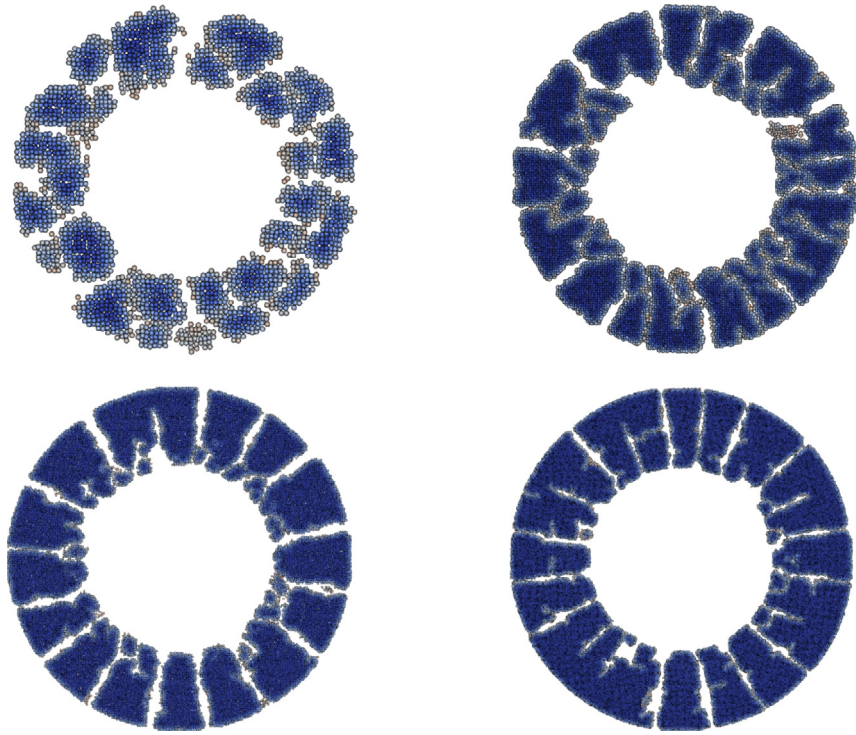


Fig. 15. Predicted fragmentation of a cylinder under internal pressure at $T = 0.2$ ms, with different discretization resolutions. Left top: 3124 particles. Right top: 12 587 particles. Left bottom: 22 413 particles. Right bottom: 35 035 particles. (For interpretation of the references to color in this figure legend, the reader is referred to the web version of this article.)

numerical simulations with 12 500–39 000 particles. This suggests the current scheme is appropriate for handling blast loading predictions, and provides consistent predictions as resolution is refined.

7. Conclusion and future work

Peridynamics presents a flexible framework for modeling fracture mechanics. In particular, bond-based fracture models admit a sharp representation of fracture surfaces while avoiding the loss of mass associated with damage models and element death [73]. This flexibility comes with a cost however, as the free-surface introduced during fracture compounds traditional challenges in peridynamic models related to nonlocal boundary conditions. This work has presented a complete workflow demonstrating for linearly elastic material how quadrature, boundary and traction loading may be handled in such a way that one preserves a limit to the relevant local problem as resolution is increased. This is a major contribution to the field of peridynamics — while numerous works have demonstrated the flexibility of peridynamics in modeling a diverse set of physical phenomena, comparatively few have demonstrated rigorous notions of convergence and grid independence. Rigorous accuracy guarantees are fundamental to trusting predictions made by numerical models, and this work aims to provide an important first step toward putting peridynamics on the same footing as e.g. finite element methods for local mechanics.

The primary focus of this work has been to establish schemes, quadrature rules, and boundary treatment and provide rigorous mathematical analysis. While numerical examples have been provided at a level appropriate for establishing the scheme's feasibility for practical problems, an important next step is to generate a performant parallel implementation allowing one to consider high-resolution predictions in two and three dimensions. For several of the validation studies provided here we were unable to reach the resolution used by other state-of-the-art peridynamic discretizations due to memory limitations of our serial implementation. The method itself is embarrassingly parallelizable, as the generation of quadrature weights and dilatation corrections involves

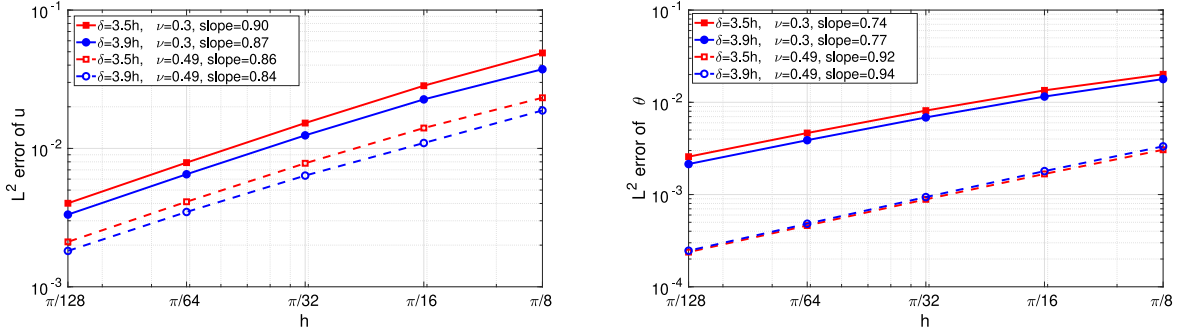


Fig. A.16. Linear patch test with uniform discretizations: traction loads applied on boundary including a corner. Left: $L^2(\Omega)$ errors of displacement u . Right: $L^2(\Omega)$ errors of dilatation θ . (For interpretation of the references to color in this figure legend, the reader is referred to the web version of this article.)

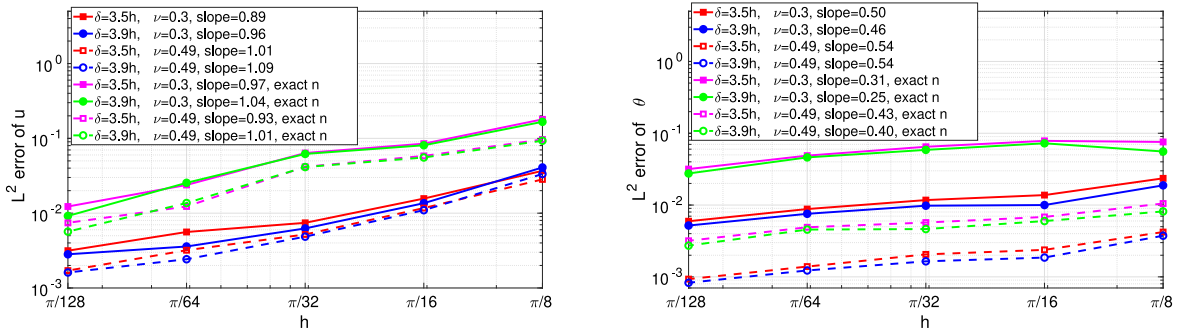


Fig. A.17. Linear patch test with non-uniform discretizations: traction loads applied on a straight line. Left: $L^2(\Omega)$ errors of displacement u . Right: $L^2(\Omega)$ errors of dilatation θ . (For interpretation of the references to color in this figure legend, the reader is referred to the web version of this article.)

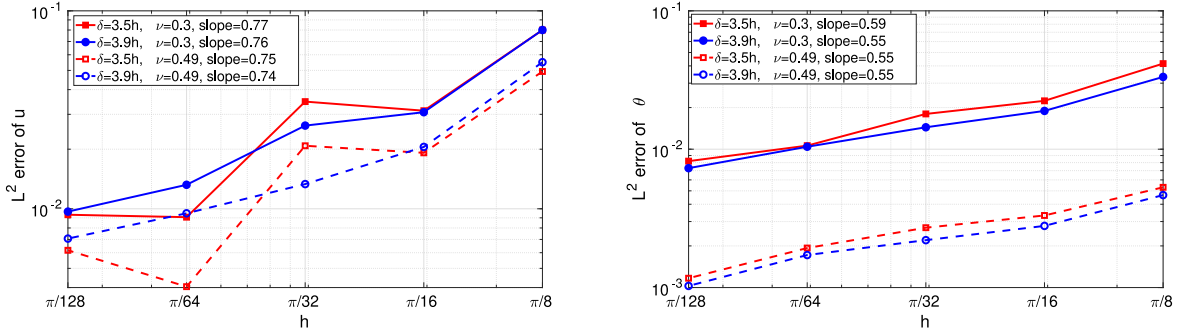


Fig. A.18. Linear patch test with non-uniform discretizations: traction loads applied on boundary including a corner. Left: $L^2(\Omega)$ errors of displacement u . Right: $L^2(\Omega)$ errors of dilatation θ . (For interpretation of the references to color in this figure legend, the reader is referred to the web version of this article.)

only the local construction and inversion of small linear matrices. In an upcoming work we will provide a clear demonstration of how the convergence guarantees provided by our approach translates to improved prediction accuracy for realistic problems. We will additionally consider the generalization of this approach to nonlinear elastoplasticity governing ductile failure.

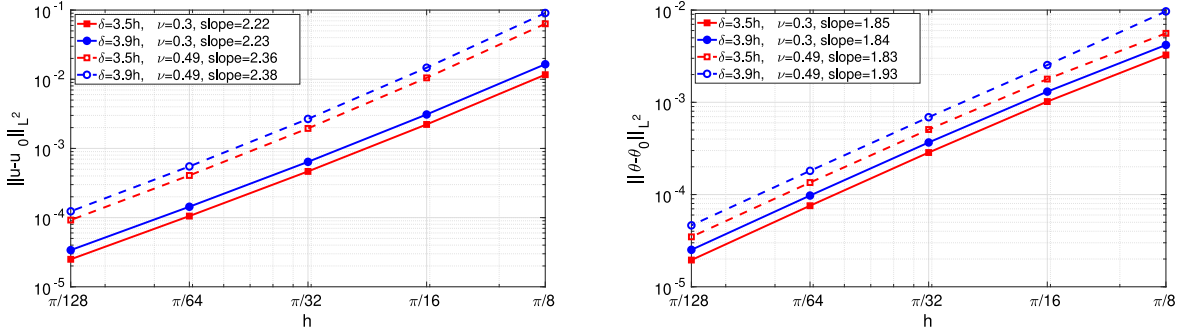


Fig. A.19. M-convergence tests on a square domain with uniform discretizations and full Dirichlet-type boundary conditions. Left: the $L^2(\Omega)$ difference between displacement u and its local limit u_0 . Right: the $L^2(\Omega)$ difference between the nonlocal dilatation θ and its local limit $\theta_0 = \nabla \cdot u_0$. (For interpretation of the references to color in this figure legend, the reader is referred to the web version of this article.)

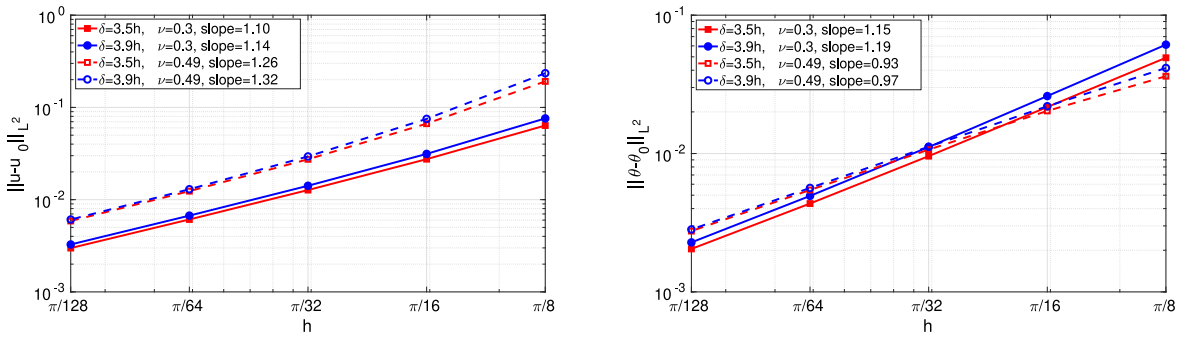


Fig. A.20. M-convergence tests on a square domain with uniform discretizations and traction loads applied on a straight line. Left: the $L^2(\Omega)$ difference between displacement u and its local limit u_0 . Right: the $L^2(\Omega)$ difference between the nonlocal dilatation θ and its local limit $\theta_0 = \nabla \cdot u_0$. (For interpretation of the references to color in this figure legend, the reader is referred to the web version of this article.)

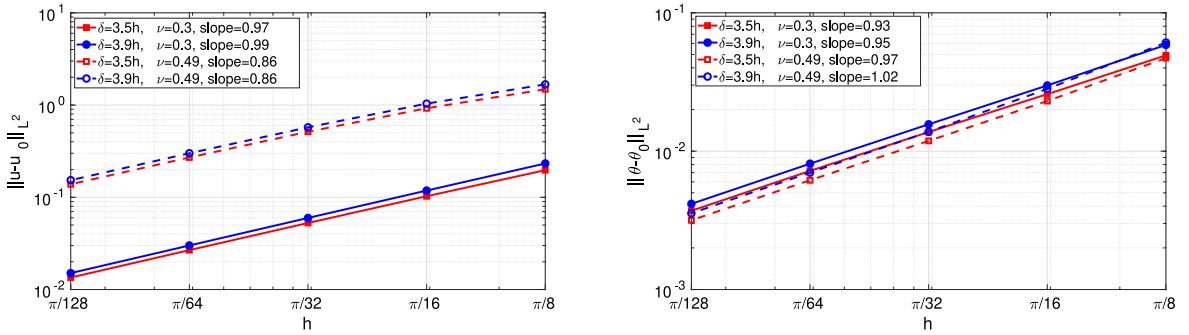


Fig. A.21. M-convergence tests on a square domain with uniform discretizations and traction loads applied on boundary including a corner. Left: the $L^2(\Omega)$ difference between displacement u and its local limit u_0 . Right: the $L^2(\Omega)$ difference between the nonlocal dilatation θ and its local limit $\theta_0 = \nabla \cdot u_0$. (For interpretation of the references to color in this figure legend, the reader is referred to the web version of this article.)

Declaration of competing interest

The authors declare that they have no known competing financial interests or personal relationships that could have appeared to influence the work reported in this paper.

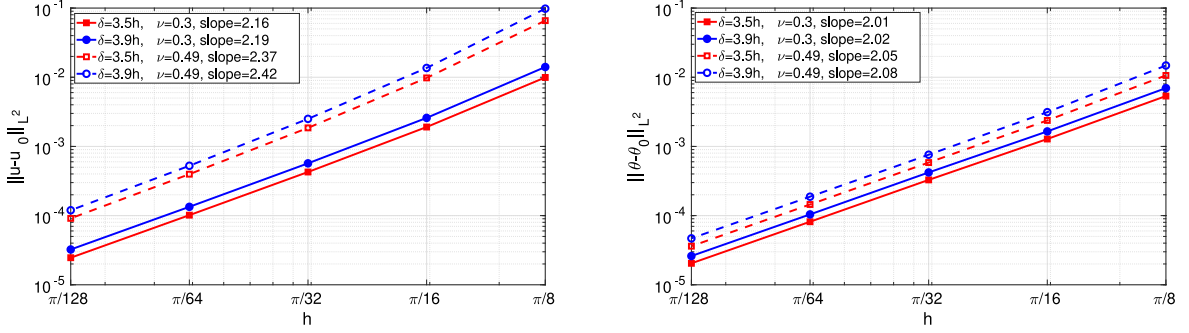


Fig. A.22. M-convergence tests on a square domain with non-uniform discretizations and full Dirichlet-type boundary conditions. Left: the $L^2(\Omega)$ difference between displacement u and its local limit u_0 . Right: the $L^2(\Omega)$ difference between the nonlocal dilatation θ and its local limit $\theta_0 = \nabla \cdot u_0$. (For interpretation of the references to color in this figure legend, the reader is referred to the web version of this article.)

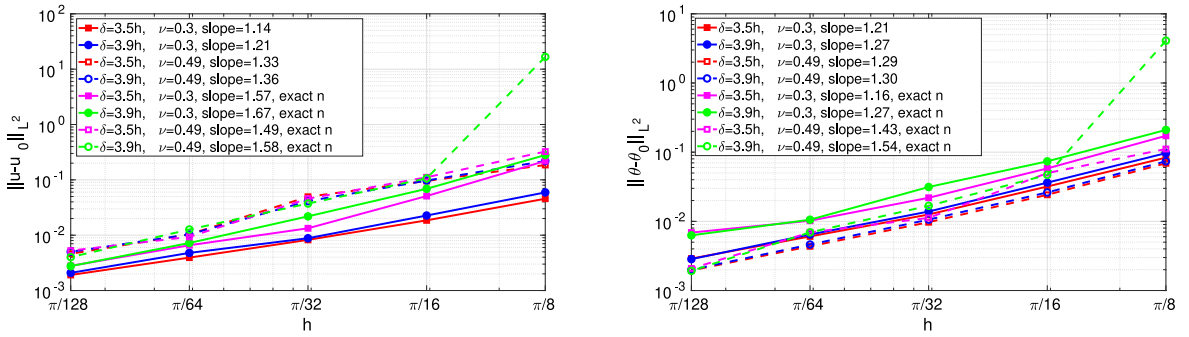


Fig. A.23. M-convergence tests on a square domain with non-uniform discretizations and traction loads applied on a straight line. Left: the $L^2(\Omega)$ difference between displacement u and its local limit u_0 . Right: the $L^2(\Omega)$ difference between the nonlocal dilatation θ and its local limit $\theta_0 = \nabla \cdot u_0$. (For interpretation of the references to color in this figure legend, the reader is referred to the web version of this article.)

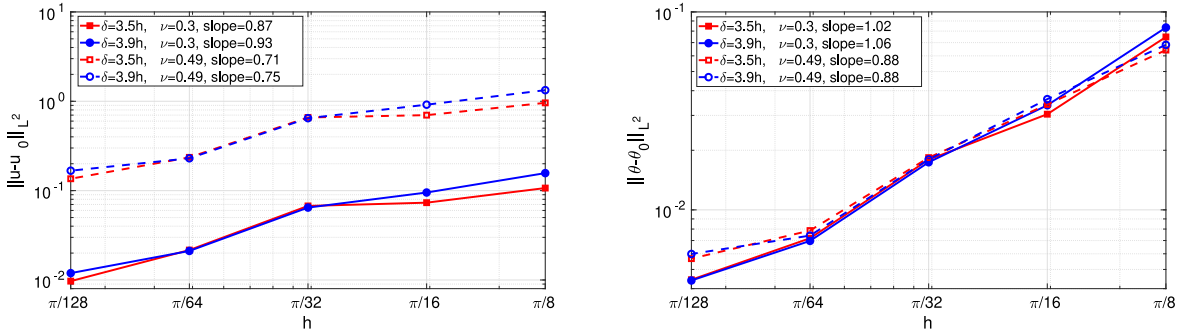


Fig. A.24. M-convergence tests on a square domain with non-uniform discretizations and traction loads applied on boundary including a corner. Left: the $L^2(\Omega)$ difference between displacement u and its local limit u_0 . Right: the $L^2(\Omega)$ difference between the nonlocal dilatation θ and its local limit $\theta_0 = \nabla \cdot u_0$. (For interpretation of the references to color in this figure legend, the reader is referred to the web version of this article.)

Acknowledgments

Sandia National Laboratories is a multi-mission laboratory managed and operated by National Technology and Engineering Solutions of Sandia, LLC., a wholly owned subsidiary of Honeywell International, Inc., for the U.S. Department of Energy's National Nuclear Security Administration under contract DE-NA0003525. This paper

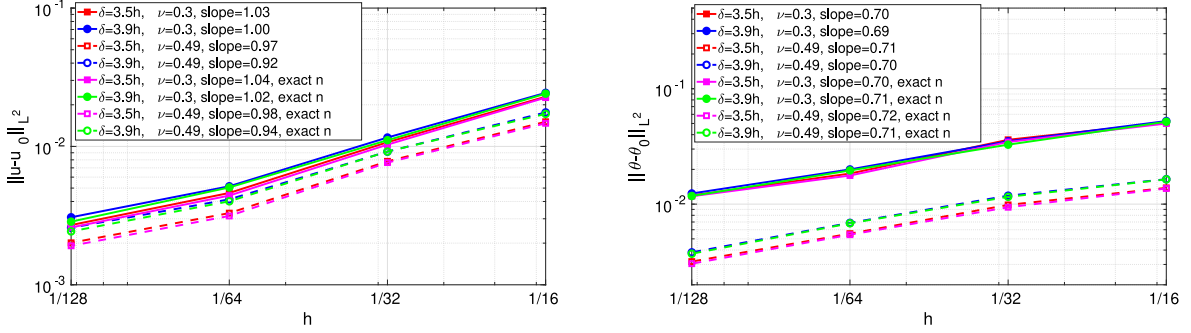


Fig. A.25. M-convergence tests for a free-surface circular hole under remote loading with uniform discretizations. Left: the $L^2(\Omega)$ difference between displacement \mathbf{u} and its local limit \mathbf{u}_0 . Right: the $L^2(\Omega)$ difference between the nonlocal dilatation θ and its local limit $\theta_0 = \nabla \cdot \mathbf{u}_0$. (For interpretation of the references to color in this figure legend, the reader is referred to the web version of this article.)

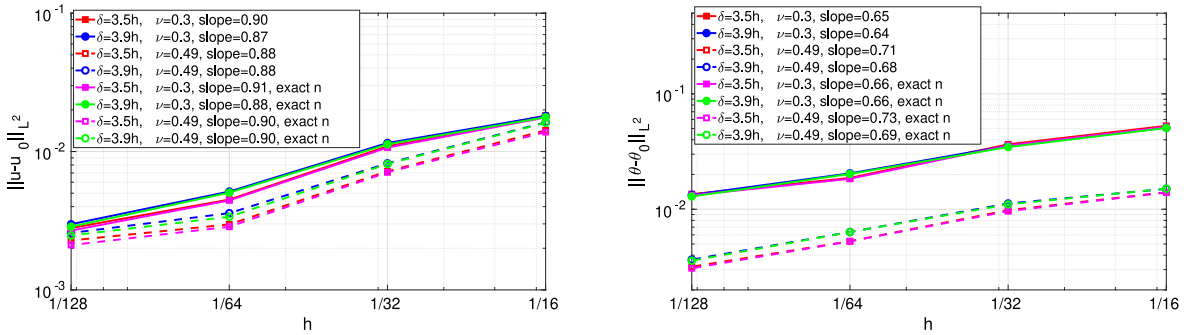


Fig. A.26. M-convergence tests for a free-surface circular hole under remote loading with non-uniform discretizations. Left: the $L^2(\Omega)$ difference between displacement \mathbf{u} and its local limit \mathbf{u}_0 . Right: the $L^2(\Omega)$ difference between the nonlocal dilatation θ and its local limit $\theta_0 = \nabla \cdot \mathbf{u}_0$. (For interpretation of the references to color in this figure legend, the reader is referred to the web version of this article.)

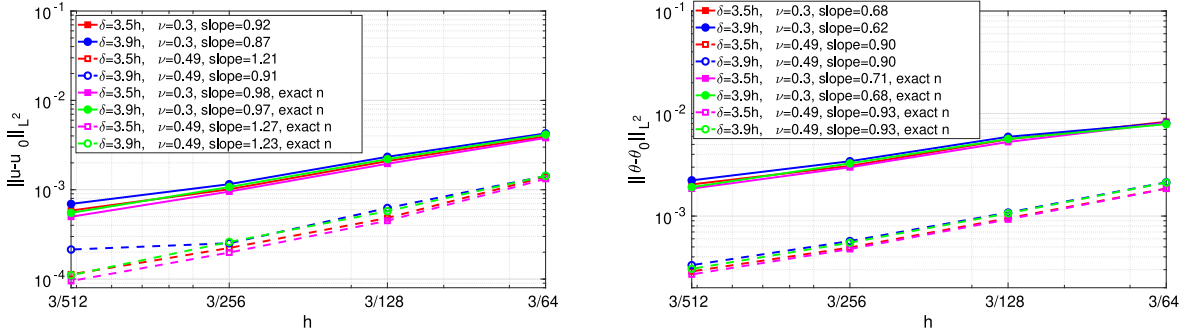


Fig. A.27. M-convergence tests for a hollow disk under internal pressure with uniform discretizations. Left: the $L^2(\Omega)$ difference between displacement \mathbf{u} and its local limit \mathbf{u}_0 . Right: the $L^2(\Omega)$ difference between the nonlocal dilatation θ and its local limit $\theta_0 = \nabla \cdot \mathbf{u}_0$. (For interpretation of the references to color in this figure legend, the reader is referred to the web version of this article.)

describes objective technical results and analysis. Any subjective views or opinions that might be expressed in the paper do not necessarily represent the views of the U.S. Department of Energy or the United States Government.

H. You and Y. Yu are supported by the National Science Foundation, United States of America under award DMS 1753031. N. Trask's work is supported under the Sandia National Laboratories, United States of America Laboratory Directed Research and Development (LDRD) program, and by the U.S. Department of Energy, Office of Science, United States of America, Office of Advanced Scientific Computing Research, United States of America

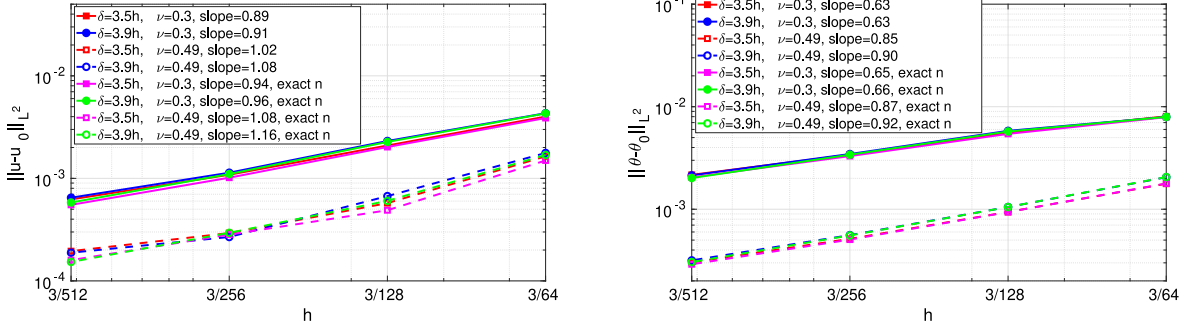


Fig. A.28. M-convergence tests for a hollow disk under internal pressure with non-uniform discretizations. Left: the $L^2(\Omega)$ difference between displacement u and its local limit u_0 . Right: the $L^2(\Omega)$ difference between the nonlocal dilatation θ and its local limit $\theta_0 = \nabla \cdot u_0$. (For interpretation of the references to color in this figure legend, the reader is referred to the web version of this article.)

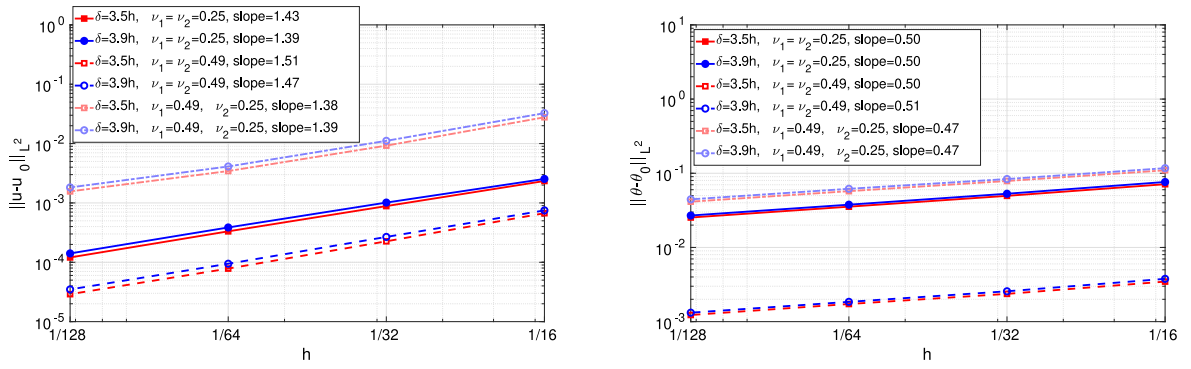


Fig. A.29. M-convergence tests for composite materials with uniform discretizations. Left: the $L^2(\Omega)$ difference between displacement u and its local limit u_0 . Right: the $L^2(\Omega)$ difference between the nonlocal dilatation θ and its local limit $\theta_0 = \nabla \cdot u_0$. (For interpretation of the references to color in this figure legend, the reader is referred to the web version of this article.)

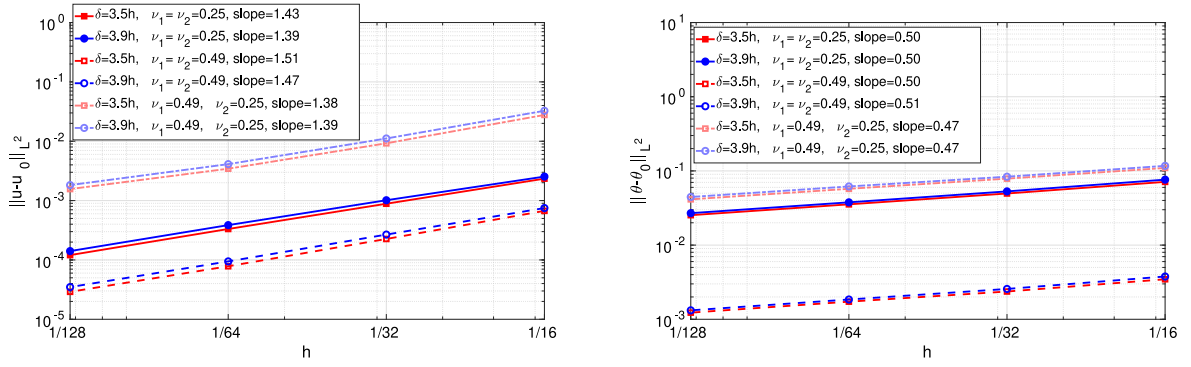


Fig. A.30. M-convergence tests for composite materials with non-uniform discretizations. Left: the $L^2(\Omega)$ difference between displacement u and its local limit u_0 . Right: the $L^2(\Omega)$ difference between the nonlocal dilatation θ and its local limit $\theta_0 = \nabla \cdot u_0$. (For interpretation of the references to color in this figure legend, the reader is referred to the web version of this article.)

under the Collaboratory on Mathematics and Physics-Informed Learning Machines for Multiscale and Multiphysics Problems (PhILMs) project. SAND number: SAND2021-0063 O.

Appendix. Convergence studies

A.1. Linear patch tests

See Figs. A.16–A.18.

A.2. Manufactured solution test

See Figs. A.19–A.24.

A.3. Traction loads on curvilinear free surfaces

See Figs. A.25–A.28.

A.4. Composite materials with discontinuous material properties

See Figs. A.29 and A.30.

References

- [1] S.A. Silling, Reformulation of elasticity theory for discontinuities and long-range forces, *J. Mech. Phys. Solids* 48 (1) (2000) 175–209.
- [2] P. Seleson, M.L. Parks, M. Gunzburger, R.B. Lehoucq, Peridynamics as an upscaling of molecular dynamics, *Multiscale Model. Simul.* 8 (1) (2009) 204–227.
- [3] M.L. Parks, R.B. Lehoucq, S.J. Plimpton, S.A. Silling, Implementing peridynamics within a molecular dynamics code, *Comput. Phys. Comm.* 179 (11) (2008) 777–783.
- [4] M. Zimmermann, A Continuum Theory with Long-Range Forces for Solids (Ph.D. thesis), Massachusetts Institute of Technology, 2005.
- [5] E. Emmrich, O. Weckner, Analysis and numerical approximation of an integro-differential equation modeling non-local effects in linear elasticity, *Math. Mech. Solids* 12 (4) (2007) 363–384.
- [6] Q. Du, K. Zhou, Mathematical analysis for the peridynamic nonlocal continuum theory, *ESAIM Math. Model. Numer. Anal.* 45 (02) (2011) 217–234.
- [7] F. Bobaru, J.T. Foster, P.H. Geubelle, S.A. Silling, *Handbook of Peridynamic Modeling*, CRC Press, 2016.
- [8] Z.P. Bažant, M. Jirásek, Nonlocal integral formulations of plasticity and damage: survey of progress, *J. Eng. Mech.* 128 (11) (2002) 1119–1149.
- [9] Q. Du, M. Gunzburger, R.B. Lehoucq, K. Zhou, A nonlocal vector calculus, nonlocal volume-constrained problems, and nonlocal balance laws, *Math. Models Methods Appl. Sci.* 23 (03) (2013) 493–540.
- [10] X. Tian, Q. Du, Asymptotically compatible schemes and applications to robust discretization of nonlocal models, *SIAM J. Numer. Anal.* 52 (4) (2014) 1641–1665.
- [11] M. D’Elia, Q. Du, C. Glusa, M. Gunzburger, X. Tian, Z. Zhou, Numerical methods for nonlocal and fractional models, 2020, arXiv preprint [arXiv:2002.01401](https://arxiv.org/abs/2002.01401).
- [12] Y. Leng, X. Tian, N. Trask, J.T. Foster, Asymptotically compatible reproducing kernel collocation and meshfree integration for nonlocal diffusion, 2019, arXiv preprint [arXiv:1907.12031](https://arxiv.org/abs/1907.12031).
- [13] M. Pasetto, Y. Leng, J.-S. Chen, J.T. Foster, P. Seleson, A reproducing kernel enhanced approach for peridynamic solutions, *Comput. Methods Appl. Mech. Engrg.* 340 (2018) 1044–1078.
- [14] M. Hillman, M. Pasetto, G. Zhou, Generalized reproducing kernel peridynamics: unification of local and non-local meshfree methods, non-local derivative operations, and an arbitrary-order state-based peridynamic formulation, *Comput. Part. Mech.* 7 (2) (2020) 435–469.
- [15] P. Seleson, D.J. Littlewood, Convergence studies in meshfree peridynamic simulations, *Comput. Math. Appl.* 71 (11) (2016) 2432–2448.
- [16] Q. Du, Local limits and asymptotically compatible discretizations, in: *Handbook of Peridynamic Modeling*, Chapman and Hall/CRC, 2016, pp. 87–108.
- [17] N. Trask, H. You, Y. Yu, M.L. Parks, An asymptotically compatible meshfree quadrature rule for nonlocal problems with applications to peridynamics, *Comput. Methods Appl. Mech. Engrg.* 343 (2019) 151–165.
- [18] H. You, X. Lu, N. Trask, Y. Yu, An asymptotically compatible approach for Neumann-type boundary condition on nonlocal problems, *ESAIM Math. Model. Numer. Anal.* 54 (4) (2020) 1373–1413.
- [19] H. You, Y. Yu, D. Kamensky, An asymptotically compatible formulation for local-to-nonlocal coupling problems without overlapping regions, *Comput. Methods Appl. Mech. Engrg.* 366 (2020) 113038.
- [20] Y. Tao, X. Tian, Q. Du, Nonlocal diffusion and peridynamic models with Neumann type constraints and their numerical approximations, *Appl. Math. Comput.* 305 (2017) 282–298.
- [21] S.A. Silling, E. Askari, A meshfree method based on the peridynamic model of solid mechanics, *Comput. Struct.* 83 (17–18) (2005) 1526–1535.

- [22] M. Bessa, J. Foster, T. Belytschko, W.K. Liu, A meshfree unification: reproducing kernel peridynamics, *Comput. Mech.* 53 (6) (2014) 1251–1264.
- [23] F. Bobaru, M. Yang, L.F. Alves, S.A. Silling, E. Askari, J. Xu, Convergence, adaptive refinement, and scaling in 1D peridynamics, *Internat. J. Numer. Methods Engrg.* 77 (6) (2009) 852–877.
- [24] R. Lipton, Dynamic brittle fracture as a small horizon limit of peridynamics, *J. Elasticity* 117 (1) (2014) 21–50.
- [25] M.L. Parks, P. Seleson, S.J. Plimpton, R.B. Lehoucq, S.A. Silling, Peridynamics with LAMMPS: A User Guide V0.2 Beta, Sandia National Laboratories, Albuquerque, NM, 2008.
- [26] P. Diehl, S. Prudhomme, M. Lévesque, A review of benchmark experiments for the validation of peridynamics models, *J. Peridyn. Nonlocal Model.* 1 (1) (2019) 14–35.
- [27] A. Javili, R. Morasata, E. Oterkus, S. Oterkus, Peridynamics review, *Math. Mech. Solids* 24 (11) (2019) 3714–3739.
- [28] C. Cortazar, M. Elgueta, J.D. Rossi, N. Wolanski, How to approximate the heat equation with Neumann boundary conditions by nonlocal diffusion problems, *Arch. Ration. Mech. Anal.* 187 (1) (2008) 137–156.
- [29] Y.D. Ha, F. Bobaru, Characteristics of dynamic brittle fracture captured with peridynamics, *Eng. Fract. Mech.* 78 (6) (2011) 1156–1168.
- [30] F. Bobaru, Y.D. Ha, Adaptive refinement and multiscale modeling in 2D peridynamics, *Int. J. Multiscale Comput. Eng.* 9 (6) (2011).
- [31] Q. Du, R.B. Lehoucq, A.M. Tartakovsky, Integral approximations to classical diffusion and smoothed particle hydrodynamics, *Comput. Methods Appl. Mech. Engrg.* 286 (2015) 216–229.
- [32] M. D'Elia, X. Tian, Y. Yu, A physically consistent, flexible, and efficient strategy to convert local boundary conditions into nonlocal volume constraints, *SIAM J. Sci. Comput.* 42 (4) (2020) A1935–A1949.
- [33] Q. Le, F. Bobaru, Surface corrections for peridynamic models in elasticity and fracture, *Comput. Mech.* 61 (4) (2018) 499–518.
- [34] E. Madenci, E. Oterkus, Coupling of the peridynamic theory and finite element method, in: *Peridynamic Theory and its Applications*, Springer, 2014, pp. 191–202.
- [35] E. Oterkus, *Peridynamic Theory for Modeling Three-Dimensional Damage Growth in Metallic and Composite Structures* (Ph.D. thesis), The University of Arizona, 2010.
- [36] R.W. Macek, S.A. Silling, Peridynamics via finite element analysis, *Finite Elem. Anal. Des.* 43 (15) (2007) 1169–1178.
- [37] Q. Du, Y. Tao, X. Tian, A peridynamic model of fracture mechanics with bond-breaking, *J. Elasticity* (2017) 1–22.
- [38] E. Madenci, E. Oterkus, Peridynamic theory, in: *Peridynamic Theory and its Applications*, Springer, 2014, pp. 19–43.
- [39] S. Oterkus, *Peridynamics for the Solution of Multiphysics Problems*, The University of Arizona, 2015.
- [40] R. Lipton, P.K. Jha, Classic dynamic fracture recovered as the limit of a nonlocal peridynamic model: The single edge notch in tension, 2019, arXiv preprint arXiv:1908.07589.
- [41] E. Madenci, M. Dorduncu, A. Barut, N. Phan, Weak form of peridynamics for nonlocal essential and natural boundary conditions, *Comput. Methods Appl. Mech. Engrg.* 337 (2018) 598–631.
- [42] B. Aksoylu, G.A. Gazonas, On nonlocal problems with inhomogeneous local boundary conditions, *J. Peridyn. Nonlocal Model.* (2020) 1–25.
- [43] E. Emmrich, O. Weckner, et al., On the well-posedness of the linear peridynamic model and its convergence towards the Navier equation of linear elasticity, *Commun. Math. Sci.* 5 (4) (2007) 851–864.
- [44] R. Lipton, Cohesive dynamics and brittle fracture, *J. Elasticity* 124 (2) (2016) 143–191.
- [45] P.K. Jha, R.P. Lipton, Kinetic relations and local energy balance for LEFM from a nonlocal peridynamic model, *Int. J. Fract.* 226 (1) (2020) 81–95.
- [46] R.P. Lipton, P.K. Jha, Plane elastodynamic solutions for running cracks as the limit of double well nonlocal dynamics, 2020, arXiv preprint arXiv:2001.00313.
- [47] T. Mengesha, Nonlocal Korn-type characterization of Sobolev vector fields, *Commun. Contemp. Math.* 14 (04) (2012) 1250028.
- [48] T. Mengesha, Q. Du, The bond-based peridynamic system with Dirichlet-type volume constraint, *Proc. Roy. Soc. Edinburgh Sect. A* 144 (1) (2014) 161–186.
- [49] T. Mengesha, Q. Du, Nonlocal constrained value problems for a linear peridynamic Navier equation, *J. Elasticity* 116 (1) (2014) 27–51.
- [50] G. Oger, M. Doring, B. Alessandrini, P. Ferrant, An improved SPH method: Towards higher order convergence, *J. Comput. Phys.* 225 (2) (2007) 1472–1492.
- [51] S.A. Silling, R.B. Lehoucq, Convergence of peridynamics to classical elasticity theory, *J. Elasticity* 93 (1) (2008) 13–37.
- [52] H. Wendland, *Scattered Data Approximation*, Vol. 17, Cambridge University Press, 2004.
- [53] S. Silling, R. Lehoucq, Peridynamic theory of solid mechanics, *Adv. Appl. Mech.* 44 (1) (2010) 73–166.
- [54] G.B. Folland, How to integrate a polynomial over a sphere, *Amer. Math. Monthly* 108 (5) (2001) 446–448.
- [55] P. Kuberry, P. Bosler, N. Trask, Compadre toolkit version 1.0.1, 2019, <http://dx.doi.org/10.5281/zenodo.2560287>.
- [56] B. Seibold, Minimal positive stencils in meshfree finite difference methods for the Poisson equation, *Comput. Methods Appl. Mech. Engrg.* 198 (3–4) (2008) 592–601.
- [57] S.A. Silling, E. Askari, A meshfree method based on the peridynamic model of solid mechanics, *Comput. Struct.* 83 (2005) 1526–1535.
- [58] G. Capodaglio, M. D'Elia, P. Bochev, M. Gunzburger, An energy-based coupling approach to nonlocal interface problems, *Comput. & Fluids* (2020) 104593.
- [59] N. Trask, M. Perego, P. Bochev, A high-order staggered meshless method for elliptic problems, *SIAM J. Sci. Comput.* 39 (2) (2017) A479–A502.
- [60] H. Zhang, P. Qiao, A state-based peridynamic model for quantitative fracture analysis, *Int. J. Fract.* 211 (1–2) (2018) 217–235.
- [61] F. Bobaru, G. Zhang, Why do cracks branch? A peridynamic investigation of dynamic brittle fracture, *Int. J. Fract.* 196 (1–2) (2015) 59–98.
- [62] S. Dondeti, H. Tippur, A comparative study of dynamic fracture of soda-lime glass using photoelasticity, digital image correlation and digital gradient sensing techniques, *Exp. Mech.* 60 (2) (2020) 217–233.

- [63] Y.D. Ha, F. Bobaru, Studies of dynamic crack propagation and crack branching with peridynamics, *Int. J. Fract.* 162 (1–2) (2010) 229–244.
- [64] X. Gu, Q. Zhang, X. Xia, Voronoi-based peridynamics and cracking analysis with adaptive refinement, *Internat. J. Numer. Methods Engrg.* 112 (13) (2017) 2087–2109.
- [65] X. Zhou, Y. Wang, Q. Qian, Numerical simulation of crack curving and branching in brittle materials under dynamic loads using the extended non-ordinary state-based peridynamics, *Eur. J. Mech. A Solids* 60 (2016) 277–299.
- [66] F. Bowden, J. Brunton, J. Field, A. Heyes, Controlled fracture of brittle solids and interruption of electrical current, *Nature* 216 (5110) (1967) 38–42.
- [67] M. Bußler, P. Diehl, D. Pflüger, S. Frey, F. Sadlo, T. Ertl, M.A. Schweitzer, Visualization of fracture progression in peridynamics, *Comput. Graph.* 67 (2017) 45–57.
- [68] Y. Yu, F.F. Bargos, H. You, M.L. Parks, M.L. Bittencourt, G.E. Karniadakis, A partitioned coupling framework for peridynamics and classical theory: analysis and simulations, *Comput. Methods Appl. Mech. Engrg.* 340 (2018) 905–931.
- [69] B.M. Sundaram, H.V. Tippur, Dynamic fracture of soda-lime glass: A full-field optical investigation of crack initiation, propagation and branching, *J. Mech. Phys. Solids* 120 (2018) 132–153.
- [70] J. Mehrmashhadi, M. Bahadori, F. Bobaru, Comparison of Peridynamic and Phase-Field Models for Dynamic Brittle Fracture in Glassy Materials, *engrXiv*, 2020.
- [71] T. Rabczuk, T. Belytschko, Cracking particles: a simplified meshfree method for arbitrary evolving cracks, *Internat. J. Numer. Methods Engrg.* 61 (13) (2004) 2316–2343.
- [72] N. Abd-Allah, M. El-Fadaly, M. Megahed, A. Eleiche, Fracture toughness properties of high-strength martensitic steel within a wide hardness range, *J. Mater. Eng. Perform.* 10 (5) (2001) 576–585.
- [73] K. Bathe, S. Bolourchi, S. Ramaswamy, M. Snyder, Some computational capabilities for nonlinear finite element analysis, *Nucl. Eng. Des.* 46 (2) (1978) 429–455.